

Using microstructures and TitaniQ thermobarometry of quartz sheared around garnet porphyroclasts to evaluate microstructural evolution and constrain an Alpine Fault Zone geotherm



Andrew J. Cross ^{a,*}, Steven Kidder ^b, David J. Prior ^a

^a Department of Geology, University of Otago, 360 Leith Walk, Dunedin 9056, New Zealand

^b Department of Earth & Atmospheric Science, The City College of New York, 160 Convent Avenue, New York, NY 10031, USA

ARTICLE INFO

Article history:

Received 22 October 2014

Received in revised form

5 February 2015

Accepted 19 February 2015

Available online 21 March 2015

Keywords:

Alpine Fault Zone

Porphyroclasts

Quartz

Microstructures

TitaniQ

Geotherm

ABSTRACT

Interpretations of deformation processes within ductile shear zones are often based on the characterisation of microstructures preserved in exhumed rocks. However, exhumed microstructures provide only a snapshot of the closing stages of deformation and we need ways of understanding how microstructures change through time and at what rate this occurs. To address this problem, we study optical microstructures and electron backscatter diffraction (EBSD) data from samples of quartz layers deflected around garnet porphyroclasts (which generate local stress and strain rate perturbations) during mylonitic deformation in the Alpine Fault Zone of New Zealand.

During shearing around rigid garnet porphyroclasts, quartz undergoes grain size reduction in response to locally increased stresses, while c-axes reveal increasing components of rhomb <a> and prism <a> slip, reflecting a local increase in shear strain and strain rate. TitaniQ thermobarometry and quartz microstructures suggest a rather narrow range of recorded quartz deformation temperatures around 450–500 °C, which we propose reflects the cessation of grain boundary migration driven deformation. Given that temperatures well above the brittle–ductile transition for quartz (~350 °C) are preserved, we anticipate that rapid cooling and exhumation must have occurred from the 500 °C isotherm. Ultimately, we propose a modified geotherm for the central Alpine Fault Zone hanging wall, which raises the 500 °C isotherm to 11 km depth, near the brittle–ductile transition. Our updated Alpine Fault Zone geotherm implies a hotter and weaker middle to lower crust than previously proposed.

© 2015 Elsevier Ltd. All rights reserved.

1. Introduction

Ductile shear zones localise deformation in much of the Earth, barring the upper few kilometres in which frictional processes dominate (Ramsay, 1980). To date, much research on ductile shear zones has involved the interpretation of microstructures preserved in rocks exhumed through the brittle–ductile transition zone. However, thin sections of deformed rocks provide only a snapshot of what may have been a long and complex deformation history involving changes in stress, strain rate and temperature through time (Toy et al., 2008; Haertel and Herwegh, 2014). One of the key challenges in interpreting natural rock microstructures is therefore

understanding how crystalline materials respond to non-steady state deformation conditions, and at what rate microstructures evolve.

It has been well established, through a combination of numerical modelling (Masuda and Ando, 1988; Samanta et al., 2002; Humphreys and Bate, 2003; Giera et al., 2013), analogue experiments (Ghosh, 1975; Passchier and Sokoutis, 1993) and studies of natural samples (Price, 1978; Lister and Price, 1978; Garcia Celma, 1982; Prior et al., 1990; Kenkmann and Dresen, 1998; Bestmann et al., 2006), that rigid particles (e.g. porphyroclasts) embedded in a weaker matrix generate mechanical instabilities which can perturb local stresses and strain rates. Despite this, no consensus has been reached on the effect of such heterogeneities on adjacent matrix microstructures, with studies finding evidence for the modification of either CPO (Lister and Price, 1978; Garcia Celma, 1982; Bestmann et al., 2006; Dempsey, 2010) or grain size (Prior et al., 1990; Kenkmann and

* Corresponding author. Department of Earth and Planetary Sciences, Washington University in St. Louis, 1 Brookings Drive, St. Louis, Missouri 63130, USA.

E-mail addresses: ajcross89@gmail.com (A.J. Cross), sbkidder@gmail.com (S. Kidder), david.prior@otago.ac.nz (D.J. Prior).

Dresen, 1998), while one study found little modification of either grain size or CPO (Price, 1978).

We aim to further this work by examining microstructural variation in quartz layers sheared around rigid garnet porphyroclasts during ductile deformation. Samples of garnet-bearing quartzofeldspathic mylonite have been studied through a combination of optical microscopy, electron backscatter diffraction (EBSD) and titanium-in-quartz (TitaniQ) thermobarometry. These samples were collected from the well-documented Alpine Fault Zone (AFZ) hanging wall mylonite sequence (Reed, 1964; Sibson et al., 1981; Prior et al., 1990; Little et al., 2002; Norris and Cooper, 2003; Toy et al., 2008) which has undergone continuous active deformation during exhumation from depths of up to 35 km (Norris and Toy, 2014). By assessing the rate of microstructural evolution in quartz, we aim to evaluate the range of conditions preserved by exhumed quartz microstructures. Ultimately, this information will be used to further constrain the Alpine Fault Zone geotherm proposed by Toy et al. (2010), and estimate crustal strength with depth in the Alpine Fault hanging wall.

2. Tectonic setting

The Alpine Fault is a 480 km long, oblique-reverse structure which represents the onshore segment of the Pacific–Australian plate boundary through New Zealand's South Island and forms the western boundary of the Southern Alps (Fig. 1a inset). The most recent estimates for present-day fault slip rates on the central section of the Alpine Fault are $27 \pm 4 \text{ mm yr}^{-1}$ dextral strike-slip and up to 10 mm yr^{-1} of reverse dip-slip motion, presenting approximately 70% of the Pacific–Australian plate convergence across the South Island (Norris and Toy, 2014).

The central section of the Alpine Fault Zone (AFZ) has a well-developed mylonite sequence, extending up to 1 km from the brittle-fault trace, progressing from protomylonites into mylonites and ultramylonites, with progressive overprinting of pre-mylonitic (protolith) Alpine Schist structures approaching the fault (Fig. 1b). The protomylonite-to-mylonite and mylonite-to-ultramylonite transitions are marked, respectively, by a switch from spaced to continuous foliation and smearing out of Alpine Schist fold hinges, and the destruction of foliation due to grain size reduction and phase mixing. Typically, the mylonites have a mineral assemblage of quartz-plagioclase-biotite-muscovite with accessory phases including garnet, titanite, ilmenite and calcite (Toy et al., 2008).

An average mylonitic foliation orientation of 055/45/SE suggests that the Alpine Fault dips at 45° at depth (Sibson et al., 1979). Below the base of the seismogenic zone at $10 \pm 2 \text{ km}$ (Eberhart-Phillips, 1995; Leitner et al., 2001; Boese et al., 2012), deformation is thought to be accommodated by a 1–2 km wide shear zone (Norris and Cooper, 2003). Seismological observations of a strong, listric reflector extending to 35 km depth, suggests that the Alpine Fault shallows onto a lower crustal décollement surface which underlies the Southern Alps to the east (Stern et al., 2007). This inference is supported by the observation that metamorphic grade never exceeds amphibolite facies (garnet-oligoclase zone; Grapes, 1995).

Vry et al. (2004) used garnet-biotite thermometry and garnet-plagioclase-muscovite-biotite barometry to estimate maximum P–T conditions of 600°C and 1.1 GPa immediately prior to mylonitisation. Retrogression from amphibolite to greenschist facies conditions during exhumation up the Alpine Fault ramp is recorded by chloritic infill of garnet fractures (Prior, 1993) and chlorite on shear band planes (Toy et al., 2008). However, following detailed analysis of quartz CPOs in the mylonites, Toy et al. (2008) found that quartz c-axis fabrics could not be easily explained in terms of decreasing temperatures during exhumation, since high-temperature prism $\langle a \rangle$ fabrics are retained at shallow depths, possibly because few

grains oriented for favourable basal $\langle a \rangle$ slip at lower temperatures are present. On the other hand, Kidder et al. (2014) recently analysed along-strike variations of quartz grain sizes in the Alpine Fault mylonites and identified, in addition to a dominant $>40 \mu\text{m}$ grain size population, a second, minor ($<10\%$ by volume) population of finer recrystallised grains (down to $4 \mu\text{m}$ in diameter). Using the quartz piezometer of Stipp and Tullis (2003), these grains correspond to large stresses of up to 200 MPa, which the authors attribute to post-seismic elastic loading of the mid-crust as predicted by finite-element modelling (Ellis and Stöckhert, 2004; Ellis et al., 2006). Thus, deformation at shallow, brittle–ductile transition depths is recorded by quartz in the AFZ mylonites, though this comprises only a background signal superimposed on a dominant, lower stress microstructure.

Norris and Cooper (2003) measured the thicknesses of pre-mylonitic pegmatite veins which are progressively sheared in the AFZ hanging wall, and obtained simple shear strain estimates of 12–22 in the protomylonites; 120–200 in the mylonites and 200–300 in the ultramylonites. Assuming that these strains were accumulated at a constant rate over the past 5 Myr, strain rates of 1×10^{-13} to 10^{-12} s^{-1} are obtained. This assumption is based on evidence that plate motion vectors have changed little over the past 5–8 Myr (Cande and Stock, 2004), although strain rates may have increased over this time period as a result of thermal-weakening feedback processes (Koons, 1987; Batt and Braun, 1999).

3. Sample description

We collected 12 samples of garnet-bearing quartzofeldspathic mylonites from Tatara Stream and Stony Creek within the central section of the Alpine Fault (Fig. 1a). All samples are L-S tectonites with a well-developed SE-dipping foliation and lineations defined by quartz-rodging and mica-streaks. Garnet porphyroclasts range between 1 and 5 mm in diameter and have single-crystal orientations (as revealed by EBSD analysis).

3.1. Lineation and shear direction determination

Complex lineation orientations arise from the rotation and shear of a pre-mylonitic, SW-plunging lineation by the Pacific–Australian plate motion vector trending at $065\text{--}068^\circ$ (Norris and Toy, 2014). Evidence from lineations (Toy et al., 2013) and shear bands (Gillam et al., 2013) indicates that the shear vector in the mylonites is oriented $\sim 20^\circ$ clockwise from the plate motion vector, implying an excess of dip-slip motion resulting in ductile extrusion. In most samples, we observe two or three different lineations, ranging in trend between 194° and 064° .

To identify samples in which Alpine Fault related deformation is dominant, we measured the orientation of the dominant shear direction with respect to the Pacific–Australian relative plate motion vector. The dominant shear direction was found in each sample by inspection of surfaces cut at varying azimuths, all perpendicular to the foliation. The shear direction is normal to the plane in which the apparent asymmetry of kinematic indicators flips (see Fig. 5 in Toy et al., 2012 for details). S–C' fabrics are moderately to well-developed in the AFZ mylonites and gave the best indication of shear sense.

Rotational sectioning revealed that most samples are dominated by a shear direction corresponding to AFZ deformation, such that S–C' fabrics typically show a top-to-the-west asymmetry (Fig. 1b). We excluded samples in which the dominant shear direction deviated from the AFZ shear vector at $\sim 090^\circ$ (Toy et al., 2013; Gillam et al., 2013) by more than 25° .

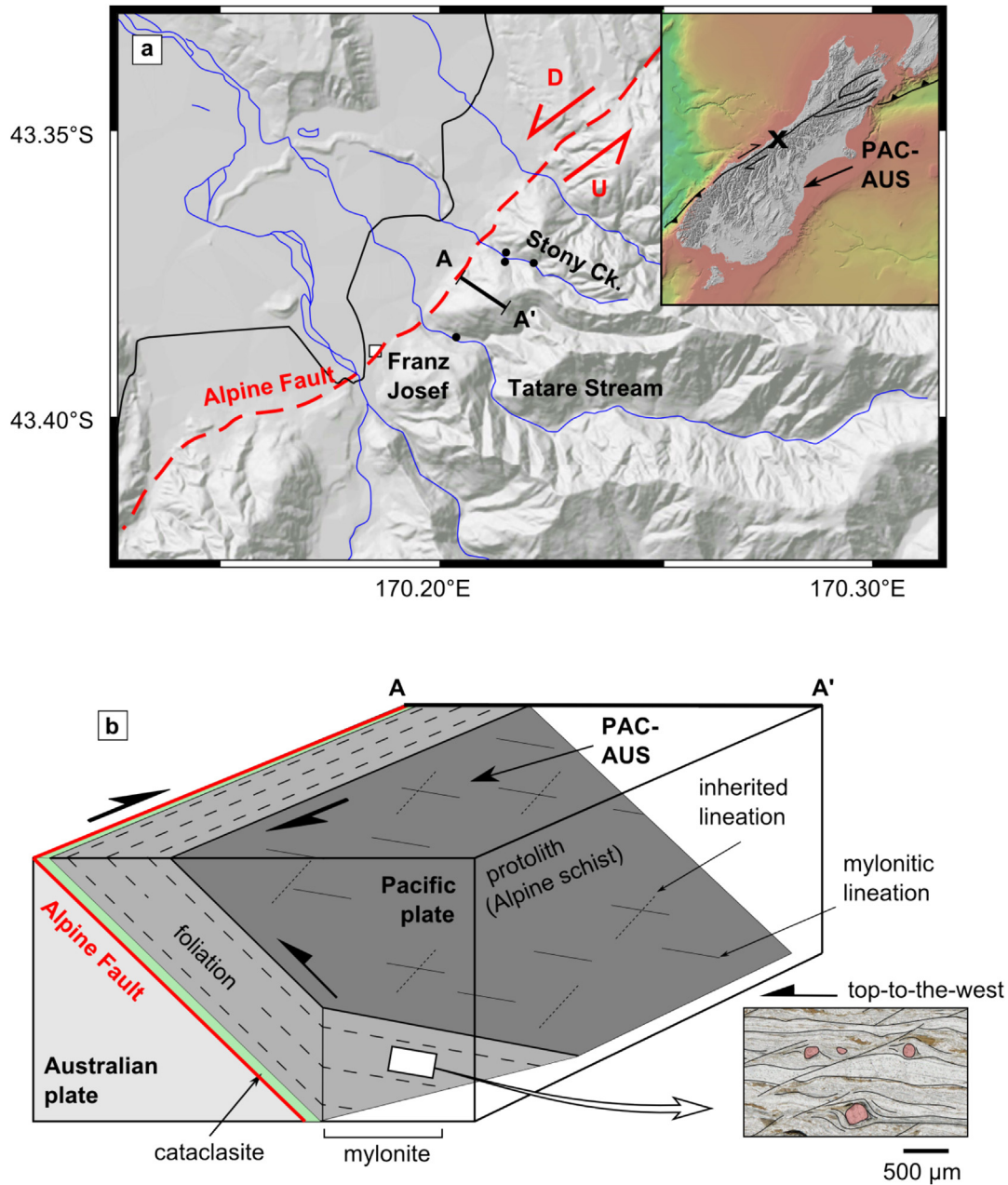


Fig. 1. (a) Tectonic setting of the Southern Alps and Alpine Fault Zone, with sample locations marked by dots in Tatara Stream and Stony Creek. (b) Schematic block diagram of the central Alpine Fault Zone, with an annotated micrograph showing the typical S–C' fabric and garnet porphyroclasts.

4. Imaging and analytical techniques

Thin sections of 30 μm thickness were prepared perpendicular to foliation and parallel with determined shear direction. Samples with garnet porphyroclasts wrapped on at least one side by quartz layers were chosen for analysis. Of our 12 samples, five were selected on the basis of their dominant shear direction and this criterion (see Table 1). Thin sections were polished using colloidal silica and coated with carbon to reduce the effects of charging during SEM imaging (Prior et al., 1999).

4.1. Electron backscatter diffraction (EBSD)

EBSD mapping was carried out using an Oxford Instruments NordlysF EBSD camera fitted to a Zeiss SIGMA VP FEG-SEM,

operating at 30 kV accelerating voltage and 90 nA beam current, at a working distance of 22 mm. Sample STO-2-03 was mapped in a Hitachi FE-SEM SU-70 SEM, operating at 20 kV and fitted with a Nordlys Nano EBSD detector. Data were collected by automatic beam rastering over a square grid with step sizes varying between 2 and 5 μm . We utilised automated stage movement to map the full lateral extent of quartz layer deflection. EBSD pattern acquisition and automatic indexing were done using the AZtec software by Oxford Instruments.

4.1.1. Data processing

Raw EBSD data were processed using the MTEX toolbox for MATLAB (Bachmann et al., 2010). MTEX converts indexed pixels to grains using a Voronoi decomposition method (for more details see Bachmann et al., 2011). Grains were defined as areas encompassed

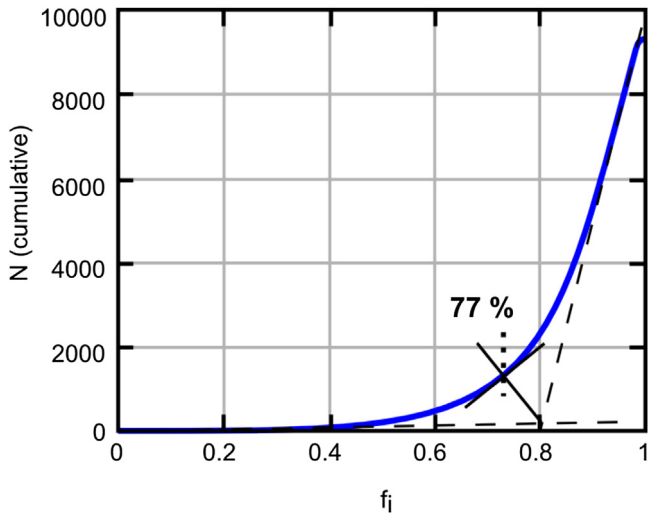


Fig. 2. A trade off curve for the indexed fraction, f_i of grains versus the cumulative number of grains, N . The knee in the curve yields a critical threshold for discriminating between well and poorly constrained grains, in this case 77%.

by boundaries of $>10^\circ$ misorientation, in accordance with TEM observations in quartz by White (1977) and Shigematsu et al. (2006). Mapped ‘grains’ smaller than 2×2 pixels are likely to result from misindexing and were removed. Though this removal introduces a skew into grain size measurements, its effect is small since the cutoff grain size is roughly an order of magnitude smaller than the mean recrystallised grain size of our samples.

To recover the maximum amount of non-indexed pixels, we allow MTEX to completely populate the mapped region with grains, rather than retaining non-indexed pixels. This approach yields well-constrained grains in densely indexed regions, but also introduces grains of unrealistic geometry in areas with poor coverage of indexed pixels. Removing these grains based on their number of indexed pixels would also remove small but well constrained grains. Instead, we remove grains using a new method based on the fraction of their area covered by raw data, f_i :

$$f_i = \frac{n_i \cdot d_{\text{step}}^2}{A_{\text{grain}}} \quad (1)$$

where for each grain, n_i is the number of indexed pixels, d_{step} is the width of each pixel (i.e. the step size), and A_{grain} is the area of that grain as constructed by MTEX. An example script for implementing this method can be found in the [supplementary material](#).

We choose a critical threshold value of f_i for the exclusion of poorly constrained grains using a trade-off curve (Fig. 2), where the knee in the curve represents the cut-off between populations of well constrained and poorly constrained grains. Typical cut-off values range between 0.5 and 0.8 (i.e. 50–80 % indexed).

4.1.2. Fabric quantification

To represent spatial variation and evolution of grain size and crystal orientation, the deflected quartz layer in each sample mapped by EBSD was subdivided into several ‘domains’ (see Figs. 5–7). Each domain contains at least 200 grains, to sufficiently sample the entire orientation space when constructing one-point-per-grain pole figures.

To quantify changes in the crystallographic orientations of quartz, we employ three methods for measuring the strength and shape of pole figures. As a measure of fabric strength, we calculate both the M-index of Skemer et al. (2005) and the J-index of Bunge

(1982). To represent the shape of crystallographic fabrics we apply the eigenvalue method of Woodcock (1977), which takes the eigenvalues of the orientation tensor and compares their magnitudes to derive a fabric shape. We express this as a log K value where $K = \ln(e_1/e_2)/\ln(e_2/e_3)$. For girdle fabrics, $\log K < 0$, while clustered fabrics yield $\log K > 0$. Grain shape preferred orientations (SPO) are also calculated from EBSD maps by automatically fitting an ellipse to each grain and measuring the angle between the ellipse long axis and bulk foliation orientation (i.e. the sample x-axis; Fig. 8).

4.2. Titanium-in-quartz (TitaniQ) thermobarometry

Titanium-in-quartz (TitaniQ) thermobarometry is a relatively new tool in assessing the temperature- and pressure-sensitive substitution of Ti for Si in quartz (Wark and Watson, 2006; Thomas et al., 2010; Huang and Audétat, 2012). Here we apply the TitaniQ method to estimate deformation temperatures in our samples and investigate the sensitivity of Ti concentrations to recrystallisation.

Ti concentrations in quartz were measured along deflected quartz layers in two samples. Samples were analysed at the California Institute of Technology, with a Cameca 7f Secondary Ion Mass Spectrometer (SIMS) using a $^{16}\text{O}^-$ primary ion beam. We used a beam current of 10–15 nA, a mass resolving power of ~ 4000 , field aperture of 100 μm , and analysed masses ^{27}Al , ^{30}Si , ^{44}Ca , ^{47}Ti , ^{49}Ti . Prior to each analysis, a $50 \times 50 \mu\text{m}$ area was rastered for 60 s. Effective spot size for the analyses was $\sim 10 \mu\text{m}$. We used a regression line constrained through the origin to calculate Ti concentrations using National Institute of Standards (NIST) glasses 610 and 612 (434 ± 15 and 44 ± 5 ppm TiO_2 respectively; Jochum et al., 2005). To account for matrix effects between quartz and NIST glass, a correction factor of 0.67, as determined by Behr et al. (2011) and independently tested by Kidder et al. (2013), was applied for the Ti data. As a Ti-blank, we used Herkimer ‘Diamond’, a natural quartz containing 4–5 ppb Ti (Kidder et al., 2013). Analyses of this natural blank suggest an effective detection limit in this study of 78 ± 27 ppb. No blank correction was made since this value is far below Ti concentrations measured in this study. Up to 70 spots were analysed in each sample. In some cases, grains were of a similar diameter to the spot size and the beam intersected grain boundaries. Kidder et al. (2013) compared Ti concentrations measured across cracks with those measured in the interior of grains and found no significant disparity. Based on their evidence, we have not discarded measurements taken across grain boundaries.

We have applied the thermobarometers of both Thomas et al. (2010) (Eq. (2)) and Huang and Audétat (2012) (Eq. (3)):

$$RT \ln X_{\text{TiO}_2}^{\text{quartz}} = -60952 + 1.520T - 1741P + RT \ln a_{\text{TiO}_2} \quad (2)$$

$$\log_{10} \text{Ti} = -2794.3/T - 660.53 \left(P^{0.35} / T \right) + 5.6459 \quad (3)$$

where R is the gas constant, $X_{\text{TiO}_2}^{\text{quartz}}$ is the mole fraction of TiO_2 in quartz, T is temperature (K), P is pressure (kbar), $\log_{10} \text{Ti}$ is the logarithm of Ti concentration in ppm and a_{TiO_2} is the TiO_2 activity. In rutile-absent systems a_{TiO_2} is anticipated to range from 0.6 to 1 (Ghent and Stout, 1984). Based on the presence of ilmenite in our samples, we set $a_{\text{TiO}_2} = 0.8$, in accordance with Ti activity estimates for metapelites (Ghent and Stout, 1984) and ilmenite-bearing rocks (Peterman and Grove, 2010; Menegon et al., 2011; Spear et al., 2012). For a_{TiO_2} errors of ± 0.2 , temperature errors are, at most, ± 30 $^\circ\text{C}$.

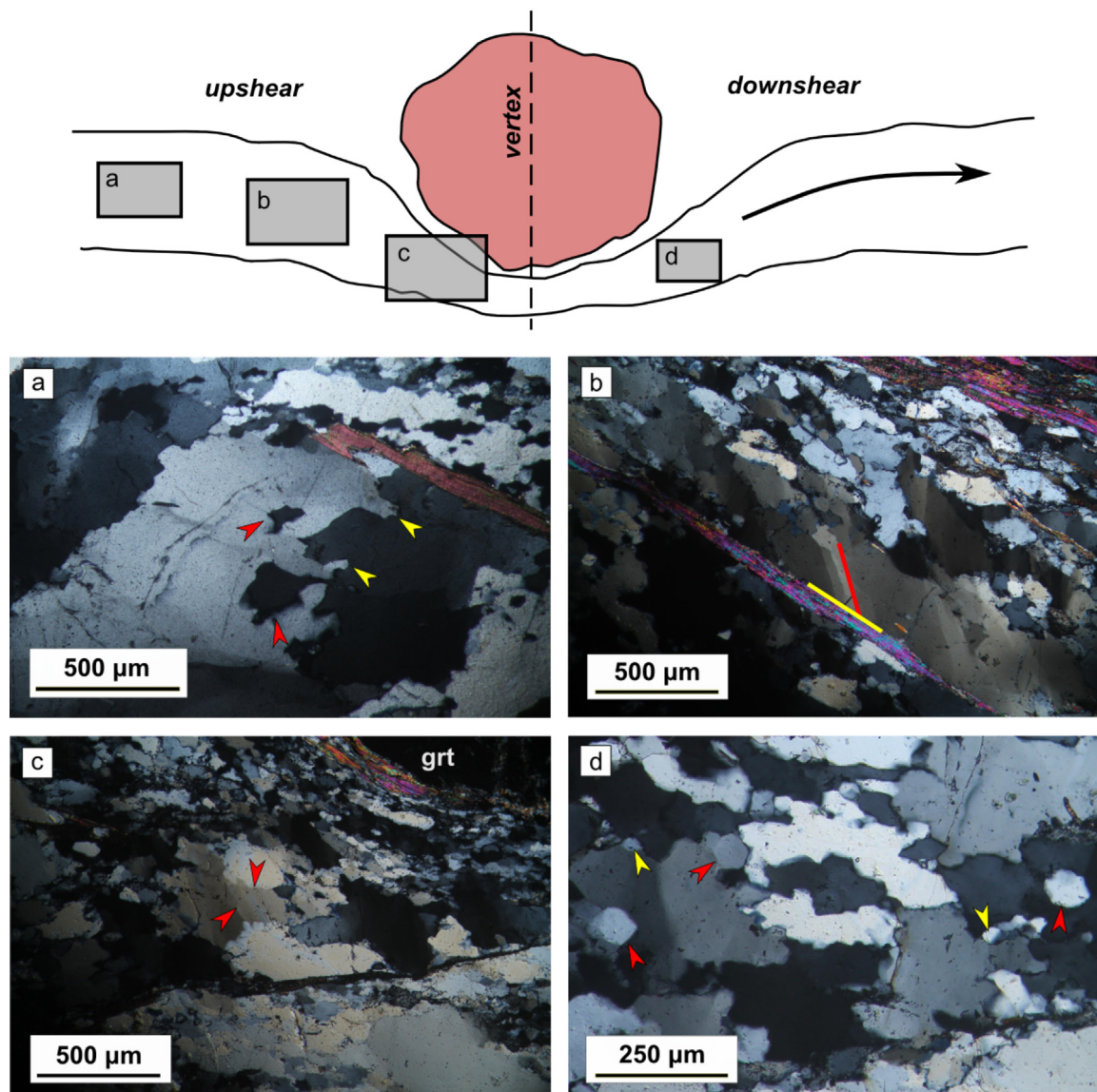


Fig. 3. A range of typical quartz microstructures observed in the Alpine Fault Zone mylonites. All images have a top-to-the-left shear sense (rightwards transport direction). (a) Large (≤ 2 mm) blocky quartz grains with patchy and undulose extinction, typical of the protomylonites, have lobate (yellow arrows) grain boundaries. Some small grains (red arrows) are preserved in the interiors of larger grains. (b) With the transition from protomylonitic to mylonitic samples, large blocky grains are flattened and appear as ribbon grains with deformation bands (red line) at high angles to foliation (yellow line). (c) Approaching garnet porphyroclasts, internal misorientations in large grains become more pronounced and organised into subgrains and deformation bands. (d) Immediately downshear of garnet porphyroclasts, grains appear more strain free than those of equivalent size upshear. Recrystallised grains (red arrows) are polygonal and equant, and often larger than subgrains (yellow arrows), which decorate grain boundaries. (For interpretation of the references to colour in this figure legend, the reader is referred to the web version of this article.)

5. Results

In all samples, microstructures are modified adjacent to garnet porphyroclasts. Compositional layers defining the mylonitic foliation become thinned and deflected around the rigid porphyroclasts. As in [Prior et al. \(1999\)](#) and [Bestmann et al. \(2006\)](#), we assume that flow paths are parallel to the local foliation and that the shear vector lies within the foliation plane. All samples are displayed here with a sinistral, top-to-the-west shear sense, consistent with [Fig. 1b](#).

In describing the spatial variation of microstructural properties, we will refer to regions either 'upshear' or 'downshear' of the garnet porphyroclast. The transition from upshear to downshear occurs at the 'layer vertex': the point at which the quartz layer reaches its point of maximum deflection. The layer vertex often coincides with a median line oriented perpendicular to the bulk foliation and bisecting the garnet porphyroclast ([Fig. 3](#)).

5.1. Quartz microstructures

[Fig. 3](#) highlights some of the typical Alpine Fault Zone quartz microstructures observed in our samples. Upshear of garnet porphyroclasts, quartz layers are dominated by large grains, up to 2000 μm in diameter. These grains, which appear blocky in the protomylonites ([Fig. 3a](#)), become progressively flattened and take on ribbon morphologies through the transition into the mylonites ([Fig. 3b](#)), with long axes at low angles ($< 20^\circ$) to the local foliation orientation. Grain boundaries are often very lobate (high-amplitude and undulatory), though in some cases become linear where quartz grains abut against foliation-parallel, tabular mica grains ([Fig. 3b](#)). Large grains are often internally strained, with extinction appearing undulose, banded or patchy ([Fig. 3a, b and c](#), respectively). Internal variations in extinction become more pronounced approaching porphyroclasts, accompanying a general decrease in grain size.

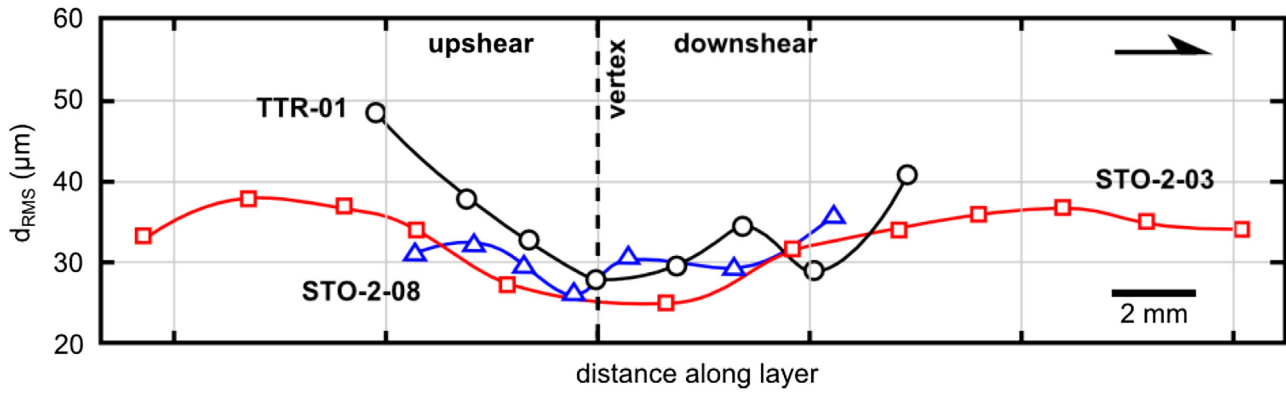


Fig. 4. Root mean square (RMS) grain sizes along quartz layers. Each measurement corresponds to the centroid of an analysed domain (where markers correspond to those shown in Figures 5, 6 and 7. The vertical line in the centre of the plot marks the layer vertex. Transport direction is to the right.

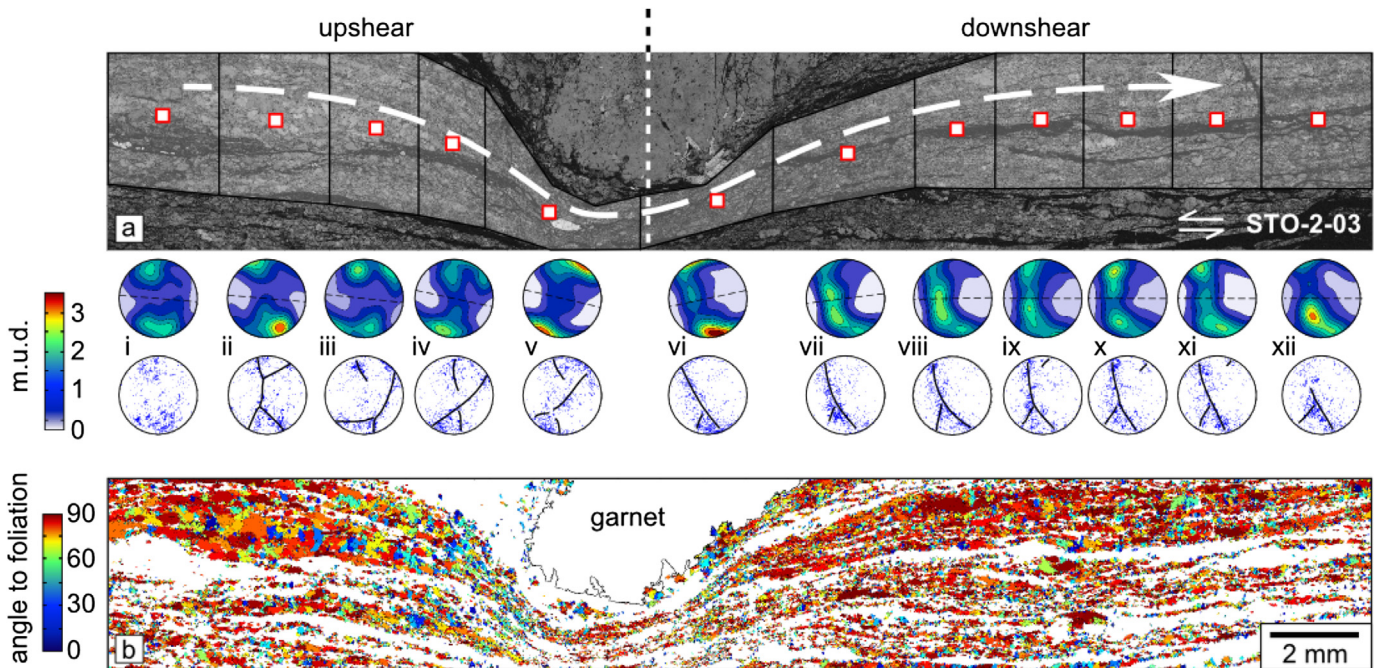


Fig. 5. Microstructural components for sample STO-2-03. (a) A band contrast (pattern quality) map, where lighter pixels represent better EBSD patterns. Domains of quartz used for microstructural analysis are outlined in black, with point data and contoured pole figures of c-axis orientations (one point per grain) shown for each (m.u.d. = multiples of uniform distribution). The dashed line through each pole figure approximates the local foliation orientation. Where fabric skeletons can be recognised, they have been drawn on point pole figures. Red squares mark the domain centroids, and correspond to symbols shown in Fig. 4. (b) Shape preferred orientation of quartz grains. Colours correspond to the angle between grain long axes and the bulk foliation plane (horizontal), where blue and red grains are at high and low angles to the foliation, respectively. (For interpretation of the references to colour in this figure legend, the reader is referred to the web version of this article.)

At the layer vertex and immediately downshear of porphyroclasts, quartz layers are comprised of grains with little internal distortion and serrated (low-amplitude and undulatory) grain boundaries decorated by subgrains which are often smaller than adjacent polygonal recrystallised grains (Fig. 3d). Moving further downshear of porphyroclasts, grain sizes increase and large blocky or ribbon grains become more abundant, such that the microstructure becomes indistinguishable from that upshear.

5.2. Grain size and shape

Grain size is defined here from EBSD data as the diameter of an area-equivalent circle. Grain size distributions in each sample follow a log-normal distribution typical for mylonites (Ranalli, 1984). We isolate recrystallised grains from larger relict grains using a grain size cutoff, defined by the knee in a tradeoff curve (similar to that shown in Figure 2) of cumulative number of grains

Table 1
Details of analysed samples.

Sample	Type	Location	Map distance from fault trace (m)	Diameter of garnet (mm)	% Quartz in layer
STO-2-02	Mylonite	Stony Creek	360	3.2	75
STO-2-03	Mylonite	Stony Creek	400	5.0	83
TTR-01	Protomylonite	Tatare Stream	720	2.9	91
TTR-02	Protomylonite	Tatare Stream	720	3.5	94
STO-2-08	Protomylonite	Stony Creek	990	2.7	87

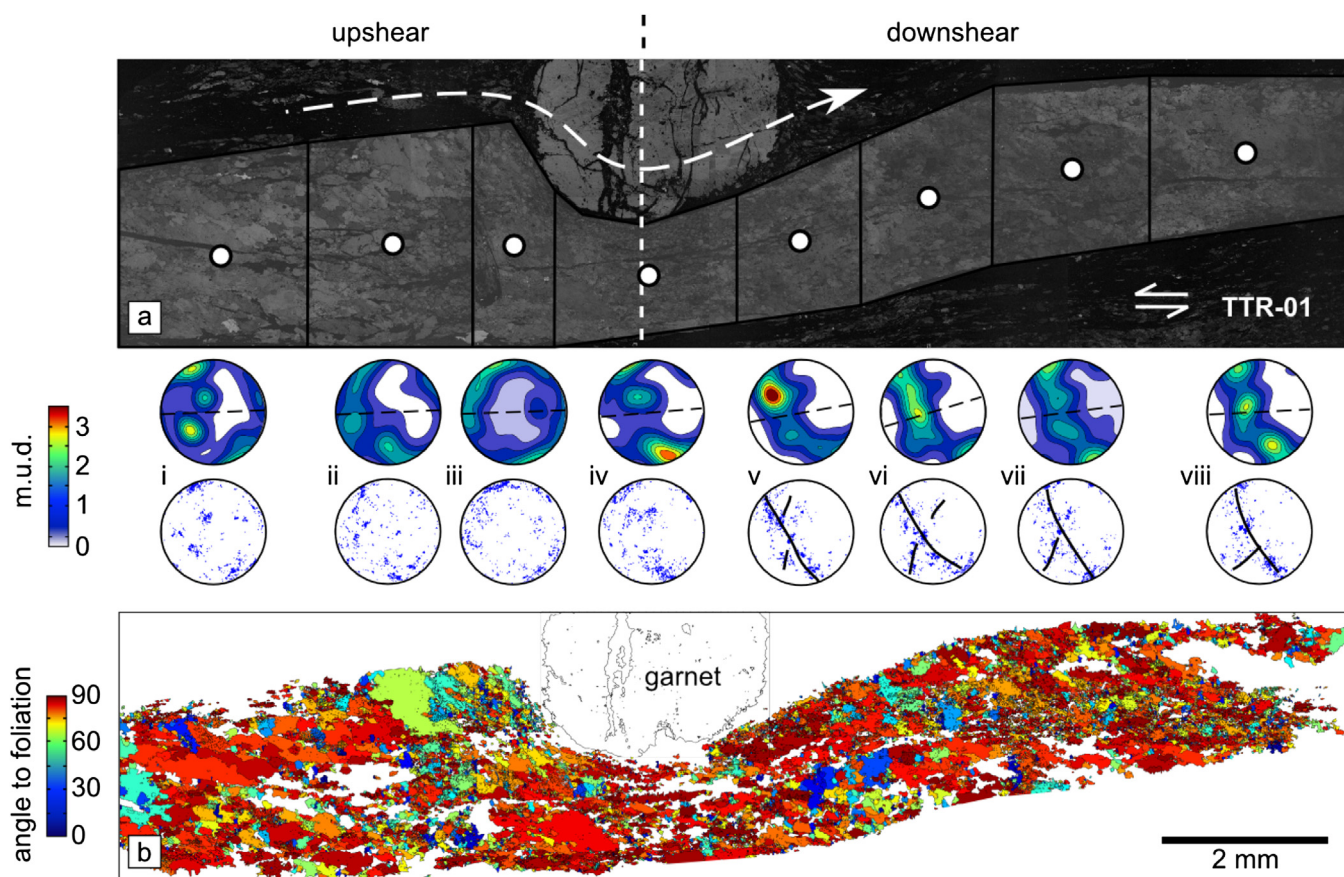


Fig. 6. Microstructural components for sample TTR-01. (a) A band contrast (pattern quality) map, where lighter pixels represent better EBSD patterns. Domains of quartz used for microstructural analysis are outlined in black, with point data and contoured pole figures of *c*-axis orientations (one point per grain) shown for each (m.u.d. = multiples of uniform distribution). The dashed line through each pole figure approximates the local foliation orientation. Where fabric skeletons can be recognised, they have been drawn on point pole figures. Black circles mark the domain centroids, and correspond to symbols shown in Fig. 4. (b) Shape preferred orientation of quartz grains. Colours correspond to the angle between grain long axes and the bulk foliation plane (horizontal), where blue and red grains are at high and low angles to the foliation, respectively. (For interpretation of the references to colour in this figure legend, the reader is referred to the web version of this article.)

versus grain size. To look at changes in recrystallised grain size along deflected quartz layers, we calculate the root mean square (RMS) recrystallised grain size in each map domain. Use of RMS values allows comparison on equal terms with the regime 2–3 piezometer of Stipp and Tullis (2003). Mean recrystallised grain sizes along each sample are presented in Fig. 4 and reveal grain size minima which closely coincide with the layer vertex in each sample. RMS grain sizes typically range between 25 and 40 μm .

In all samples, quartz grains define a clear shape preferred orientation (SPO) with mean aspect ratios of 1.7 ± 0.6 . Quartz grain long axes are inclined at low angles (typically less than 15°) to the bulk foliation plane orientation. SPO variations along each sample are minimal, though we do observe a small zone of weaker SPO upshear and immediately adjacent to the garnet in each of our three samples (Figs. 5b, 6b and 7b).

5.3. Crystallographic fabric

To understand the evolution of crystallographic preferred orientation (CPO) during deformation of quartz around a rigid body, we have measured quartz *c*-axis orientations in the same domains used for quantifying grain size. Pole figures were constructed using one point per grain to prevent a grain size bias on orientation density function (ODF) calculation, and are presented as lower hemisphere, equal area stereographic projections of both point and contoured point data (15° smoothing cone half-width), using the reference frame shown in Fig. 8. The same reference

frame (with the bulk sample foliation in the *X–Y* plane) was used for all pole figures, rather than being rotated to match locally deflected foliation orientations.

As grains are progressively sheared around porphyroclasts, we observe an evolution of *c*-axis fabrics. In sample STO-2-03 (Fig. 5), weakly asymmetric cross-girdles of type-1 (as defined by Lister and Hobbs, 1980) dominate the upshear part of the quartz layer (Fig. 5; pole figures i–iv). Near the layer vertex, there is a strengthening and rotation of these girdles about the kinematic vorticity axis (Fig. 5; pole figures v–vi) as more strongly asymmetric cross-girdles develop (Fig. 5; pole figure vii). The rotation of *c*-axis girdles is consistent with the top-to-the-west shear sense inferred in each sample from macroscopic kinematic indicators.

C-axis pole figures for sample TTR-01 display a similar progression towards rotated and strengthened cross girdles (Fig. 6; pole figures v–viii), from weak girdles and clusters in the *X–Z* plane (plane of the thin section) upshear (Fig. 6; pole figure iii).

STO-2-08 *c*-axis distributions are weak, owing to a paucity of data, and the orientation space is therefore poorly sampled. However, *Z*-maxima orientations are evident (Fig. 7; pole figure iii) and cross-girdles are weakly formed in some pole figures (Fig. 7; pole figures i–ii).

In Fig. 9a and b, we present two scalar measures of fabric strength: the *J*-index of Bunge (1982) and the *M*-index of Skemer et al. (2005). Both of these measures show a tendency for fabric intensity to increase towards the layer vertex. In all samples, the value of fabric strength at the layer vertex is a factor of 1.5–2

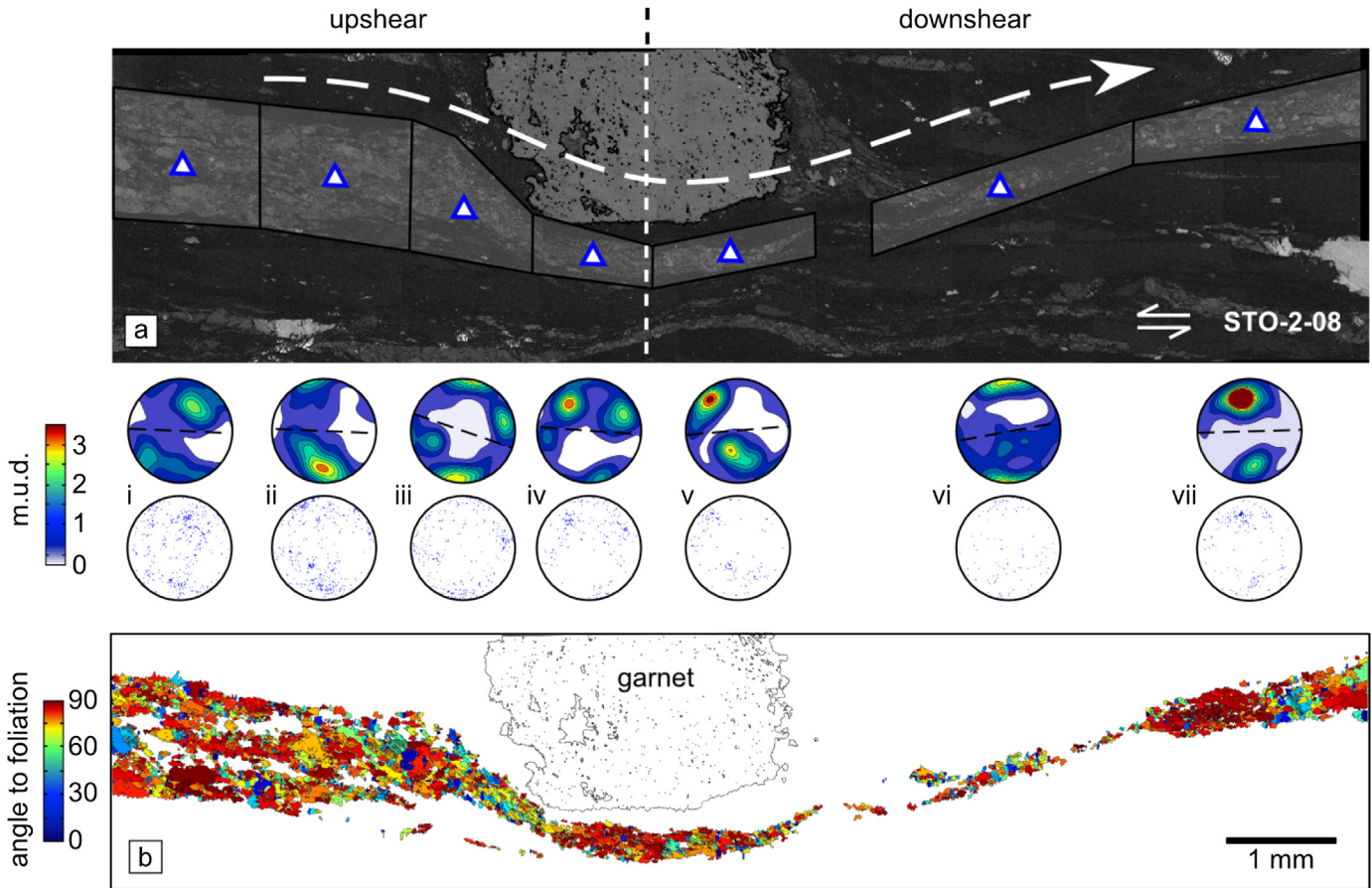


Fig. 7. Microstructural components for sample STO-2-08. (a) A band contrast (pattern quality) map, where lighter pixels represent better EBSD patterns. Domains of quartz used for microstructural analysis are outlined in black, with point data and contoured pole figures of *c*-axis orientations (one point per grain) shown for each (m.u.d. = multiples of uniform distribution). The dashed line through each pole figure approximates the local foliation orientation. Blue triangles mark the domain centroids, and correspond to symbols shown in Fig. 4. (b) Shape preferred orientation of quartz grains. Colours correspond to the angle between grain long axes and the bulk foliation plane (horizontal), where blue and red grains are at high and low angles to the foliation, respectively. (For interpretation of the references to colour in this figure legend, the reader is referred to the web version of this article.)

greater than that of the weakest fabric observed in each sample. Eigenvector analysis of *c*-axes (Fig. 9c) and *a*-axes (Fig. 9d) shows no common systematic trend. In general, *c*-axes have components of both girdled and clustered fabrics.

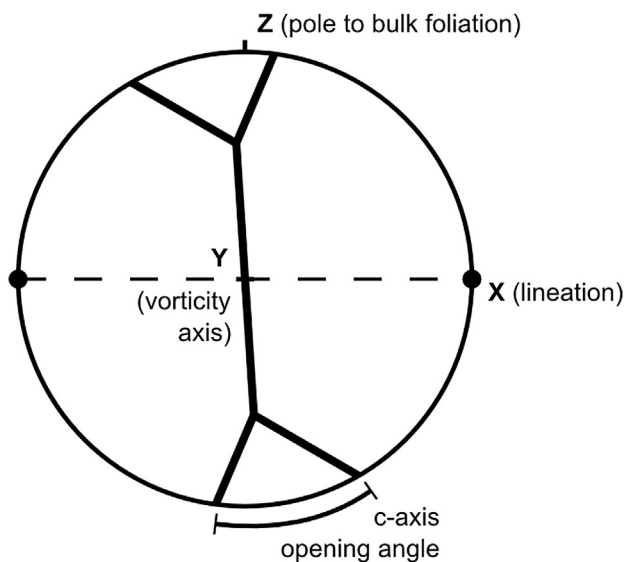


Fig. 8. Sample reference frame and fabric skeleton for an asymmetric cross-girdle.

5.4. Titanium in quartz concentrations

Ti concentrations were measured at ~70 spots in both sample STO-2-02 and TTR-01. The locations of analysed spots are plotted in Fig. 10 and coloured by their Ti concentration. In sample TTR-02 there is no clear trend in Ti concentration with distance along the quartz layer, aside from a small reduction in Ti at the layer vertex (Fig. 10a), though these concentrations are of the same magnitude as those measured in some grains upshear. Sample STO-2-02 displays lower Ti concentrations throughout the layer, though large grains upshear of the garnet have markedly higher amounts of Ti (Fig. 10b).

It has been suggested that there is a link between recrystallisation and Ti concentration, with recrystallisation able to ‘reset’ Ti concentrations in quartz (Grujic et al., 2011; Kidder et al., 2013; Nachlas et al., 2014). To explore the influence of recrystallisation on Ti concentration, we plot Ti concentration versus both grain size (Fig. 11a) and the difference in extinction angle across each grain, as a measure of intragranular lattice distortion (Fig. 11b), to distinguish recrystallised grains from relict grains (Fig. 11c). Additionally, we measure the proximity of each spot measurement to a grain boundary, since some authors have noted decreasing Ti concentrations moving from grain cores to rims (Nachlas et al., 2014). The results of this analysis reveal no significant correlation of Ti concentration with any of the three properties measured, suggesting that Ti concentrations were relatively equilibrated at the time deformation ceased. Equilibration of Ti is also suggested by a fairly

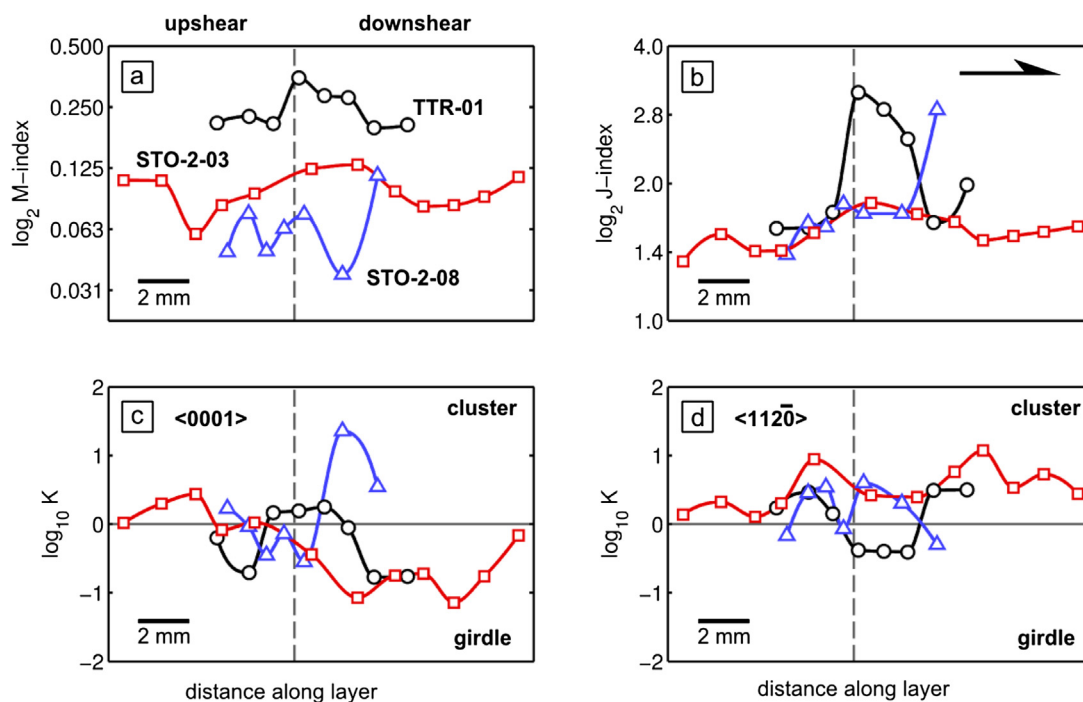


Fig. 9. Measures of fabric strength and shape. Figures (a) and (b) show the M-index (Skemer et al., 2005) and J-index (Bunge, 1982) scalar measures of fabric strength respectively. Figures (c) and (d) are ratios of the orientation tensor eigenvalues, which describe the shape of quartz (c) c-axis and (d) a-axis fabrics plotted in stereonet space. The vertical line in each plot marks the layer vertex, acting as a proxy for the point of most intense deformation.

uniform CL signal (Fig. 11d) compared to that seen in non-equilibrated rocks (e.g. Kidder et al., 2013).

6. Discussion

6.1. Kinematics

Quartz crystallographic fabrics are often used to infer deformation conditions (e.g. Schmid and Casey, 1986; Law, 2014). The strongest c-axis fabrics observed in our samples are Z-maxima and type-1 cross-girdles. Typically, c-axis girdles strengthen in the downshear direction along a deflected quartz layer (Figs. 5 and 6), owing to an increase in the number of grains deforming by rhomb $\langle a \rangle$ and prism $\langle a \rangle$ slip, relative to those deforming by basal $\langle a \rangle$ (Z-maxima) slip. Moreover, cross-girdles appear to become increasingly asymmetric in the downshear direction, particularly in sample STO-2-03 (Fig. 5; pole figures i \rightarrow vii). This trend of increasing asymmetry has been previously documented in quartzites deformed to progressively higher finite shear strains both experimentally (Heilbronner and Tullis, 2006) and naturally (Schmid and Casey, 1986). We therefore infer that the transition from symmetric to asymmetric c-axis fabrics reflects a local increase in shear strain caused by quartz layer constriction. Considering that the duration of deformation across each sample is uniform, an increase in shear strain also implies an increase in local shear strain rate adjacent to the porphyroclast. A reduction in recrystallised grain size in this region also suggests a local increase in stress, according to the often-observed inverse relationship between recrystallised grain size and differential stress (Twiss, 1977; Stipp and Tullis, 2003), although recrystallised grain size may also be a function of strain rate and temperature (Austin and Evans, 2007, 2009).

6.2. Deformation mechanisms

The mechanisms for recovery and dynamic recrystallisation in quartz can be divided into three regimes (Hirth and Tullis, 1992;

Stipp et al., 2002). Our samples contain large ($<2000 \mu\text{m}$) grains displaying increasing amounts of deformation bands and subgrain structures approaching garnet porphyroclasts, accompanying grain size reduction. Grain boundaries throughout the quartz layer, but particularly upshear, appear very lobate. Directly downshear of garnets, polygonal strain-free grains are larger than neighbouring subgrains. These microstructures are diagnostic of crystal plastic deformation by subgrain rotation recrystallisation (SGR) accompanying rapid grain boundary migration (GBM), following the classification of Stipp et al. (2002). The importance of crystal plastic processes is further highlighted by a factor of two increase in two independent measures of quartz crystallographic fabric strength adjacent to garnet porphyroclasts (Fig. 9b and c).

6.3. Deformation conditions from quartz microstructures

Much thermobarometric work has been previously been done on the Alpine Fault Zone mylonites and their protolith, the Alpine Schist (see Toy et al., 2010 and references therein). During exhumation from depths of ≤ 35 km, ductile deformation is constrained to have continued to greenschist facies conditions (Prior, 1993; Toy et al., 2008). Here we discuss how quartz microstructures and Ti concentrations can be used to assess the temperatures recorded by our samples.

The quartz deformation regimes discussed above and defined by Hirth and Tullis (1992) and Stipp et al. (2002) relate to temperature and strain rate conditions, and can therefore be used to constrain deformation conditions. Given the lobateness of quartz grain boundaries, and the apparently rapid rate of microstructural evolution (as witnessed by changes to CPO and grain size over short distances), grain boundary migration must have been an important component of deformation. The onset of GBM has been constrained in natural rocks at 450–500 °C for strain rates of $10^{-12} - 10^{-13} \text{ s}^{-1}$ (Stipp et al., 2002) appropriate for the Alpine Fault Zone. Since GBM microstructures are well preserved and minimally overprinted, we suggest that cooling from this temperature must have been

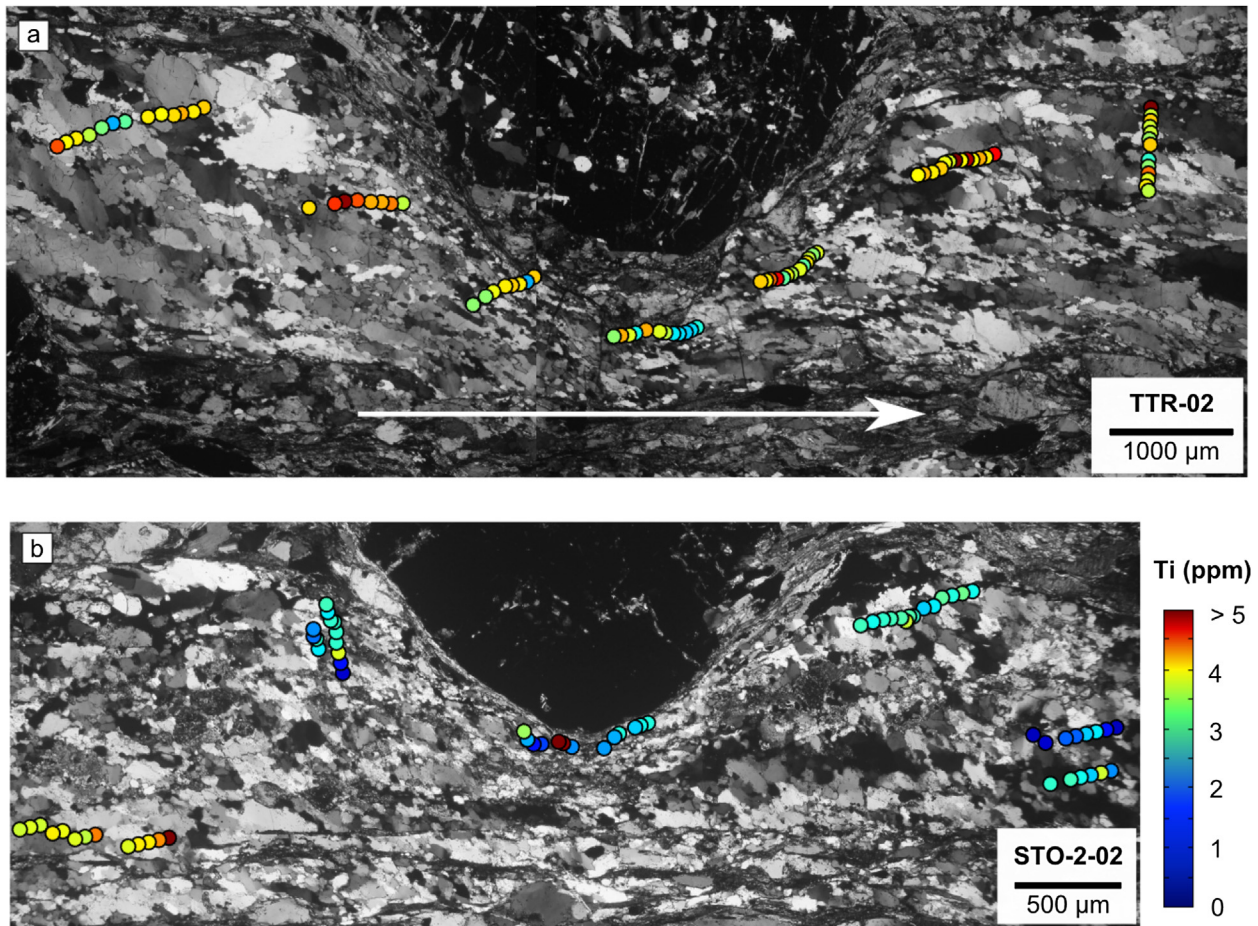


Fig. 10. Ti concentrations (ppm) in samples (a) TTR-02 and (b) STO-2-02. Both samples have a shear sense of top-to-the-left. The cross-polarised images in the background have been desaturated to better show the Ti spot colours. (For interpretation of the references to colour in this figure legend, the reader is referred to the web version of this article.)

relatively rapid. On the other hand, considering that recrystallised grains appear to have nucleated via subgrain rotation recrystallisation, some minor recrystallisation may have continued down to the BLG-SGR transition, which occurs at 370–420 °C for the same range of strain rates.

Quartz *c*-axis opening angles have also been proposed as a thermometer for quartz creep deformation (Law et al., 2004, 2010; Law, 2014). Using the *c*-axis thermometer presented by Law (2014), *c*-axis opening angles of between 50 and 60°, as observed in samples STO-2-03 and TTR-01, yield temperatures of between 400 and 500 °C. Given that the *c*-axis thermometer of Law (2014) is calibrated for strain-rates of 10^{-12} to 10^{-14} s $^{-1}$, and strain rates for the AFZ mylonites are anticipated to be within the upper end of this range, it is likely that temperatures are closer to 500 °C than 400 °C (assuming an isostress control on the opening angles of quartz *c*-axes).

6.4. Deformation temperatures from TitaniQ

Temperature estimates from quartz microstructures can be compared to those from TitaniQ thermobarometry. We obtain pressures and temperatures using both the Thomas et al. (2010) and Huang and Audétat (2012) TitaniQ calibrations (Fig. 12). In our approach we calculate temperatures based on an initial estimate of pressure and compare the corresponding depth to that given by the Toy et al. (2010) geotherm for the same temperature. Pressure is modified iteratively until temperatures and pressures converge on the geotherm.

Mean temperatures calculated for sample STO-2-02 are 342 ± 45 °C (Thomas et al. calibration), or 503 ± 62 °C (Huang and Audétat calibration). Temperatures in sample TTR-02, collected further from the Alpine Fault trace, are higher at 378 ± 27 °C (Thomas et al.), or 551 ± 29 °C (Huang and Audétat). Given that the errors associated with the uncertainty on Ti activity (± 30 °C) are of a similar magnitude to the scatter on temperatures given here, we find it likely that variations in temperatures calculated from TitaniQ can be explained by local variations in Ti activity. If this is the case, our titanium concentrations record deformation at a single temperature or narrow range of temperatures, despite the retrogressive P-T history of the AFZ mylonites.

Temperatures calculated using the Huang and Audétat (2012) calibration align with temperatures estimated from quartz SGR-GBM microstructures, while those calculated using Thomas et al. (2010) lie around the depths anticipated for the brittle–ductile transition in the central Alpine Fault Zone (Leitner et al., 2001; Toy et al., 2010). Since there is no significant link between Ti concentration and recrystallisation in our samples, we consider two possible scenarios:

1. Ti equilibrated rapidly during deformation due to fast grain boundary migration, as suggested by Grujic et al. (2011). This scenario would support the Huang and Audétat (2012) calibration, with Ti concentrations recording the cessation of GBM, as suggested by the similarity between the Huang and Audétat temperatures with the GBM-closure temperature around 450–500 °C.

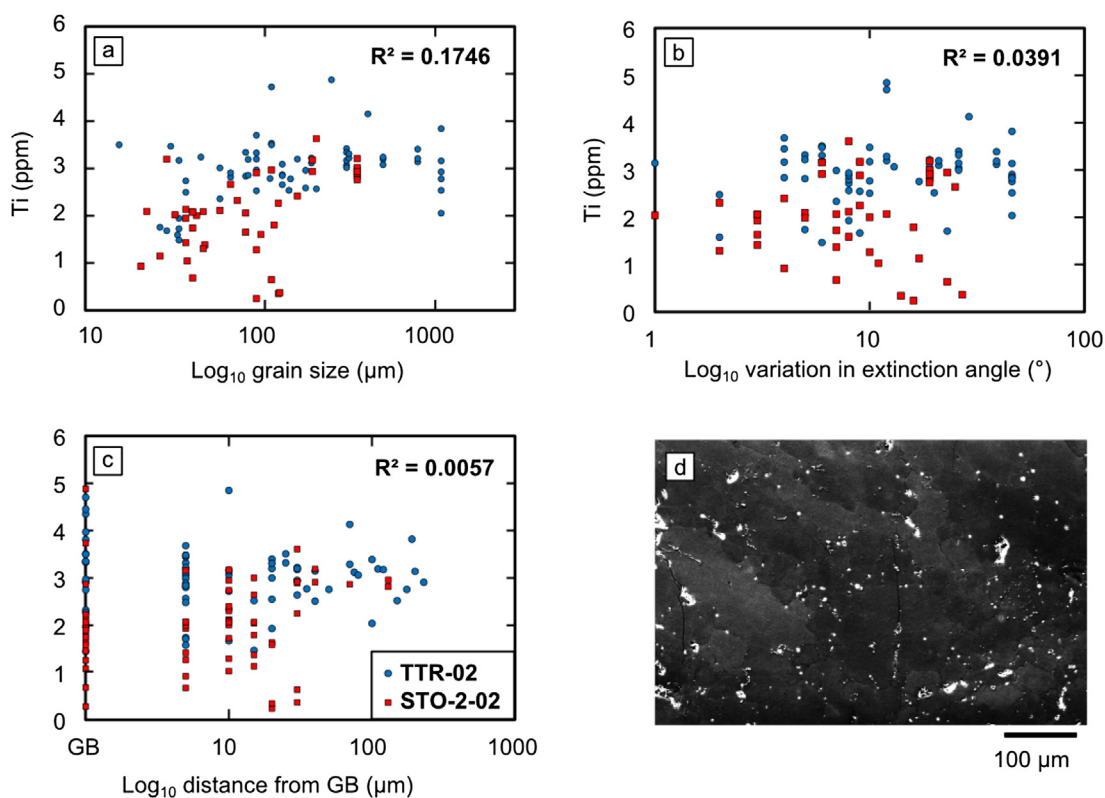


Fig. 11. Grain based analysis of Ti concentration data. We observe no significant correlation of Ti concentration with (a) grain size, (b) intragranular variation in extinction angle under cross-polarised light or (c) distance of measurements from grain boundaries. (d) is a CL image of quartz in sample STO-2-02 with a reasonably uniform intensity, though some grains have slightly higher CL brightnesses.

- Ti diffusion continued after the cessation of dynamic recrystallisation and may have continued up to the brittle–ductile transition as indicated by the cooler temperatures of Thomas et al. (2010).

However, in consideration of the latter possibility, Ti diffusion rates are slow at temperatures below 500 °C. Cherniak et al. (2007) found that at 500 °C, the characteristic diffusion length scale after one million years is 2 μm. At the rate of exhumation in the Alpine Fault Zone, it would take 2.5 Ma for rocks to be exhumed from the 500 °C isotherm at ~25 km depth to the surface, and significantly less than this time to reach temperatures at which Ti diffusion is ineffective. Thus, volume diffusion in even our recrystallised grains (25–40 μm) would be too slow to equilibrate Ti concentrations at temperatures below the SGR-GBM boundary. Other authors have also noted that re-equilibration of titanium-in-quartz is inefficient in the absence of GBM (Grujic et al., 2011; Haertel et al., 2013) and as such, deformation temperatures below ~450 °C are poorly recorded by TitaniQ thermobarometry.

6.5. Stress and strain rate estimates

We can also evaluate the validity of our temperature estimates by using rheological flow laws for quartz to predict strain rates of deformation and compare these with strain rate constraints for the Alpine Fault Zone. To do this requires an estimate of differential stress, which we obtained through recrystallised grain size paleopiezometry.

Recrystallised quartz grains in our samples are typically 25–40 μm in size. According to the quartz piezometer of Stipp and Tullis (2003), recently tested and found to be accurate at natural

conditions by Kidder et al. (2012), recrystallised grain sizes in this range correspond to differential stresses of 44 ± 8 MPa. Applying a stress of 44 MPa and the mean temperatures estimated by the two TitaniQ calibrations (360 and 525 °C) to the quartz dislocation creep flow law of Hirth et al. (2001) yields strain rate estimates of $7.8 \times 10^{-15} \text{ s}^{-1}$ and $1.79 \times 10^{-11} \text{ s}^{-1}$, for pressures and water fugacities appropriate to 8 and 29 km depth, respectively. Interestingly, both of these strain rate estimates are beyond the limits of conditions anticipated for the Alpine Fault Zone ($10^{-13} - 10^{-12} \text{ s}^{-1}$). However, we acknowledge that there is considerable uncertainty in the application of laboratory rheological flow laws to nature. To test this sensitivity, we calculate strain rate as a function of temperature in Fig. 13, using four different quartz flow laws. At temperatures of 360 °C and 525 °C, the range of strain rates from the four flow laws are $10^{-14} \pm 1.6 \text{ s}^{-1}$ and $10^{-11} \pm 1.0 \text{ s}^{-1}$, respectively. Though the strain rates are still too slow at 360 °C, the range of strain rates for 525 °C now partially overlap with strain rate estimates for the AFZ. Despite this, the true strain rates are likely to be at the upper end of this range, near the Hirth et al. (2001) and Paterson and Luan (1990) flow laws which are more likely to be accurate at natural conditions, unlike the laboratory-derived flow laws of Gleason and Tullis (1995) and Brodie and Rutter (2000). Based on this discrepancy and microstructural constraints outlined below, we consider a modification to the Alpine Fault Zone geotherm of Toy et al. (2010).

6.6. A modified Alpine Fault Zone geothermal gradient

As it stands, there are several inconsistencies between our microstructural and thermobarometric data, and the literature constraints on AFZ deformation conditions:

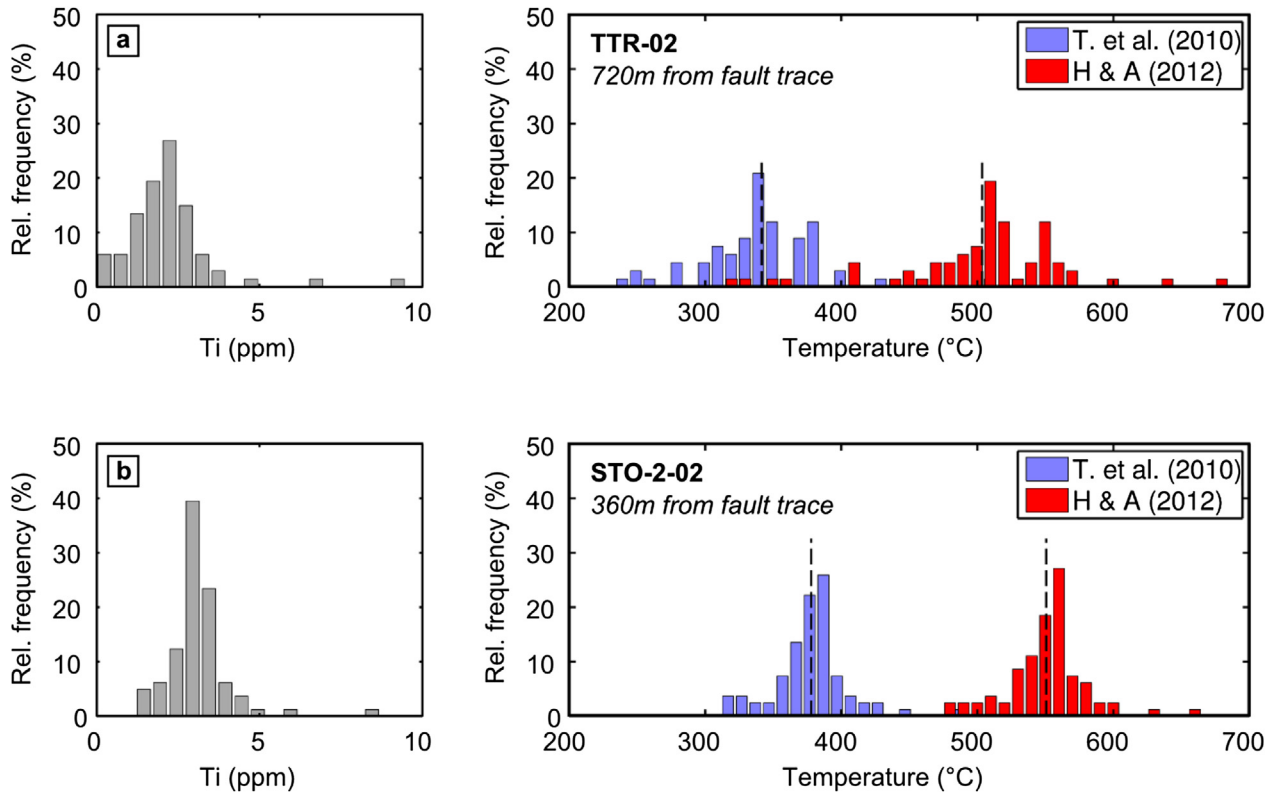


Fig. 12. Histograms of Ti concentration (in ppm) and estimated temperatures using the Thomas et al. (2010) and Huang and Audéat (2012) TitaniQ thermobarometers for samples (a) TTR-02 and (b) STO-2-02. The black dashed line on the temperature histograms represents an arithmetic mean temperature. Temperatures are constrained using the Toy et al. (2010) central Alpine Fault Zone geotherm and a pressure gradient with overburden density of 2700 kg m⁻³.

1. When taken at face value, the temperature–depth estimates from both TitaniQ calibrations are broadly scattered, covering almost the entire crust, with depths ranging from 5 to 40 km (Fig. 14).
2. Neither temperature estimates from microstructural indicators (SGR-GBM microstructures and *c*-axis opening angles) or from TitaniQ thermobarometry give reasonable strain rate conditions, when constrained by the geothermal gradient presented by Toy et al. (2010).
3. Given the rapid rates of microstructural change in quartz (Prior et al., 1990; this study) and the fact that GBM microstructures are well preserved with little overprinting, these rocks must have either cooled rapidly from ~500 °C or stopped deforming at around this temperature.

It is difficult to imagine then, how microstructures from the 500 °C isotherm at ~25 km depth (according to the Toy et al., 2010 geotherm) could be exhumed without evidence of widespread lower-temperature deformational overprinting or static annealing. These inconsistencies can be resolved by assuming that quartz microstructures and Ti concentrations were formed at around brittle–ductile transition depths immediately prior to rapid quenching in the shallow crust. Such a re-calculation requires only a minor modification of the Toy et al. (2010) geotherm. Extending an upper crustal 45 °C km⁻¹ geotherm to 11 km and reducing the lower crustal geotherm to 5 °C km⁻¹, still satisfies the thermometry data presented in Toy et al. (2010), while re-positioning the 500 °C isotherm at depths consistent with the base of seismicity in the central Alpine Fault Zone (Eberhart-Phillips, 1995; Leitner et al., 2001; Boese et al., 2012). The new geothermal gradient also increases (by a factor of 4.5) the rate of cooling from 500 to 325 °C (the critical temperature range between the apparent cessation of

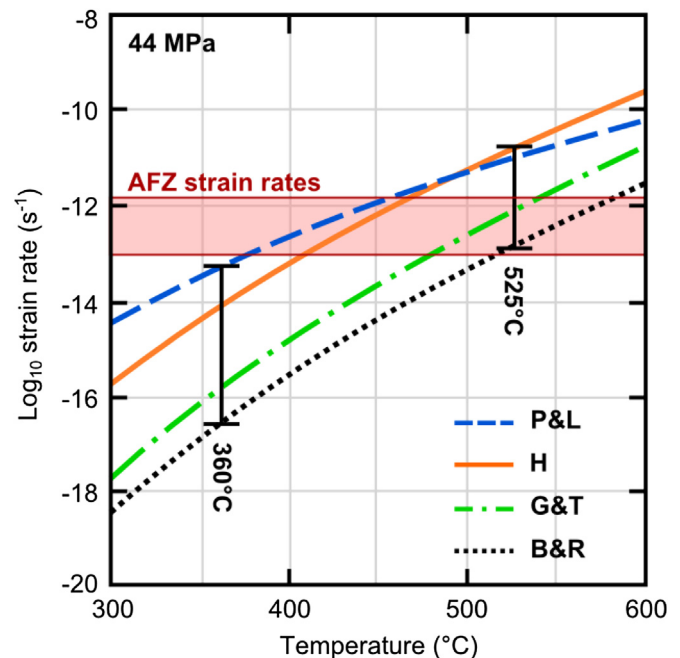


Fig. 13. A comparison of rheological flow laws for quartz creep in the AFZ and at a fixed stress of 44 MPa estimated from quartz paleopiezometry. Flow laws are: P&L – Paterson and Luan (1990); H – Hirth et al. (2001); G&T – Gleason and Tullis (1995) and B&R – Brodie and Rutter (2000). Vertical black lines represent the range of strain rates for a given temperature. For comparison, the range of strain rates expected for the Alpine Fault Zone are shown as a red shaded region. Temperatures of 360 °C and 525 °C correspond to temperatures calculated from the Thomas et al. (2010) and Huang and Audéat (2012) TitaniQ calibrations. (For interpretation of the references to colour in this figure legend, the reader is referred to the web version of this article.)

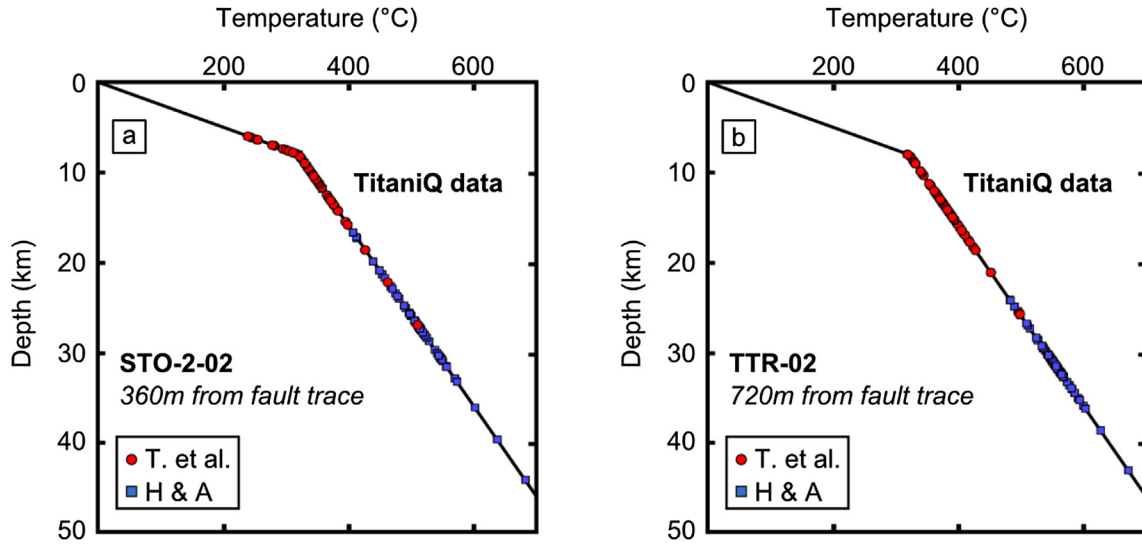


Fig. 14. Temperature–depth estimates of sample conditions from TitaniQ thermobarometry, constrained using the Toy et al. (2010) AFZ geotherm for samples (a) STO-2-02 and (b) TTR-01. A change in slope occurs at the predicted brittle–ductile transition (dashed line). H & A (2012) = Huang and Audétat (2012) TitaniQ calibration; T. et al. (2010) = Thomas et al. (2010) TitaniQ calibration.

quartz deformation and the effective cessation of quartz grain growth and creep deformation).

Using our modified geotherm to recalculate pressure and temperature estimates from TitaniQ, repositions our samples in a depth range of 7–11 km (Fig. 15a), significantly narrowing the range of predicted depths. The resulting pressure and temperature estimates now correspond to strain rates of $1.8 \times 10^{-15} \text{ s}^{-1}$ and $3.4 \times 10^{-13} \text{ s}^{-1}$ for the Thomas et al. and Huang and Audétat calibrations, largely reflecting changes in water fugacity at the shallower new depths. Though the strain rate estimate from the Thomas et al. calibration is probably far too small, based on the total strain observed and the available time for deformation, the Huang and Audétat calibration now implies strain rates which are consistent with the most recent strain rates given for the AFZ mylonites (Toy et al., 2013).

6.7. Estimates of crustal strength

We can visualise the depths recorded by our measured Ti concentrations by plotting them on a crustal strength profile using the calculated temperatures and pressures. Crustal strength profiles are commonly constructed using constitutive behaviour relationships for brittle and ductile deformation mechanisms (e.g. Kohlstedt et al., 1995). We explore the strength of the brittle upper crust using the equation of Sibson (1974) for an Andersonian strike-slip regime, and the strength of the ductile lower crust using the quartz dislocation creep flow law of Hirth et al. (2001). Dislocation creep is limited by Goetze's criterion, which states that differential stress must be lower than the effective pressure ($P_{\text{lithostatic}} - P_{\text{fluid}}$). For the Alpine Fault Zone, fluid pressures are often assumed to be hydrostatic in the seismogenic upper crust (Sibson et al., 1988; Jenkin et al., 1994; Toy

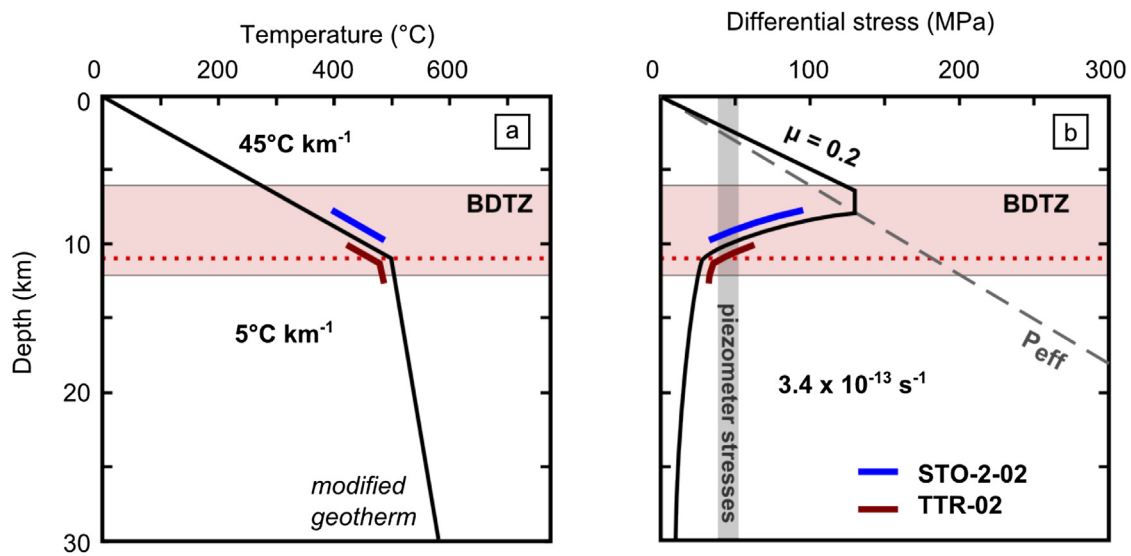


Fig. 15. Crustal strength profiles for the central Alpine Fault Zone constructed with a modified version of the Toy et al. (2010) geotherm, which places thermobarometric estimates from titanium-in-quartz close to the 500 °C isotherm at a depth of 11 km. Data plotted are representative of temperatures for samples STO-2-02 and TTR-02 (within 2 standard deviations of the mean) from the Huang and Audétat (2012) TitaniQ calibration only. The red shaded region represents the range of depths estimated for the brittle–ductile transition zone in the central AFZ, where the change in geothermal gradient at 11 km depth is shown by a red dotted line and corresponds to a kink in the creep strength curve. (For interpretation of the references to colour in this figure legend, the reader is referred to the web version of this article.)

et al., 2008, 2010). We assume a creep strain rate of $3.4 \times 10^{-13} \text{ s}^{-1}$ as discussed above, and an upper crustal friction coefficient, μ of 0.2 (Liu and Bird, 2002). These values yield a strength profile (Fig. 15) for which the zone of semi-brittle flow (transition between linear elastic and power-law creep behaviour) lies at 6–8 km depth, in a temperature range of 300–350 °C consistent with the onset of viscous creep in quartz (Tullis and Yund, 1977).

The results of our crustal strength modelling can be seen in Fig. 15, in which the stresses predicted by the quartz dislocation creep flow law (at temperatures given by TitaniQ and for a strain rate of $3.4 \times 10^{-13} \text{ s}^{-1}$) coincide with the brittle–ductile transition zone for the AFZ, and differential stresses estimated from paleo-piezometry. By raising the 500 °C isotherm to 11 km depth, we predict the middle to lower crust to be hotter and therefore rheologically weaker than implied by the Toy et al. (2010) isotherm. This is logical, considering the relatively rapid rates of uplift ($\leq 10 \text{ mm yr}^{-1}$) and fast strain rates for the Alpine Fault Zone, which should result in isotherm advection.

7. Summary

Porphyroblast systems provide useful constraints on the kinematics of deformation in ductile shear zones. Moreover, these systems provide a snapshot of microstructural adaptation to changing stresses and strain rates. We have analysed a series of samples in which quartz is ductilely sheared around garnet porphyroblasts in mylonites of the Alpine Fault Zone. Through crystallographic and thermobarometric analysis, we present the following model of mylonitic deformation during exhumation:

1. Under transpressional shear and exhumation, quartz layers are deflected around rigid garnet porphyroblasts, experiencing a local increase in shear strain rate as a result of layer thinning. Type-1 cross girdles strengthen and are rotated around the kinematic vorticity axis.
2. As quartz is transported towards a garnet porphyroblast, stresses and strain rates increase, and quartz crystal lattices become increasingly distorted, driving subgrain formation and a reduction in grain size by dynamic recrystallisation. Dominant crystal plastic deformation causes a local increase in the strength of crystallographic fabrics at the point of maximum quartz layer deflection.
3. Grains subsequently grow back to their original sizes under reducing stresses and strain rates.
4. Rates of microstructural evolution and titanium-in-quartz equilibration are fast at temperatures above ~500 °C, because of rapid grain boundary migration, which ceases between 450 and 500 °C.
5. A lack of significant microstructural overprinting by recrystallisation or grain growth below 500 °C implies rapid cooling, though grains may have continued to nucleate by subgrain rotation recrystallisation during decelerating creep down to temperatures of ~400 °C. This model requires a slight reworking of the Toy et al. (2010) geotherm, such that the transition between upper (45 °C km^{-1}) and lower (5 °C km^{-1}) geotherms occurs at a depth of 11 km.
6. Our new geotherm suggests a hotter, and therefore weaker, middle to lower crust in the hanging wall of the Alpine Fault Zone of New Zealand, consistent with rapid rates of uplift and isotherm advection.

Acknowledgements

This work was funded by a New Zealand Marsden Fund grant (number UOO1116) awarded to D.J.P., a University of Otago Doctoral

Scholarship awarded to A.J.C and National Science Foundation funding (Grant Number 1064805) for S.K. We would like to thank Eddie Dempsey for the pilot study in his thesis that provided initial direction for this work, Brent Pooley for producing high-quality thin sections and Hui Jiang at Oxford Instruments for EBSD mapping of sample STO-2-03. Thanks also to Virginia Toy and Tim Little for sharing their knowledge on the Alpine Fault Zone, and to Mike Palin, James Scott and Susan Ellis for additional helpful discussion. Water fugacities were calculated using Tony Withers' online calculator. Finally, we are grateful to Tim Little and Whitney Behr for thorough and constructive reviews, and to Cees Passchier for his assistance as journal editor.

Appendix A. Supplementary data

Supplementary data related to this article can be found at <http://dx.doi.org/10.1016/j.jsg.2015.02.012>.

References

- Austin, N.J., Evans, B., 2007. Paleowattmeters: a scaling relation for dynamically recrystallized grain size. *Geology* 35, 343–346.
- Austin, N., Evans, B., 2009. The kinetics of microstructural evolution during deformation of calcite. *J. Geophys. Res. Solid Earth* (1978–2012) 114 (B9).
- Bachmann, F., Hielscher, R., Schaeben, H., 2010. Texture analysis with MTEX—free and open source software toolbox. *Solid State Phenom.* 160, 63–68.
- Bachmann, F., Hielscher, R., Schaeben, H., 2011. Grain detection from 2d and 3d EBSD data: specification of the MTEX algorithm. *Ultramicroscopy* 111, 1720–1733.
- Batt, G., Braun, J., 1999. The tectonic evolution of the Southern Alps, New Zealand: insights from fully thermally coupled dynamical modelling. *Geophys. J. Int.* 136, 403–420.
- Behr, W.M., Thomas, J.B., Hervig, R.L., 2011. Calibrating Ti concentrations in quartz for SIMS determinations using NIST silicate glasses and application to the TitaniQ geothermobarometer. *Am. Mineral.* 96, 1100–1106.
- Bestmann, M., Prior, D.J., Grasemann, B., 2006. Characterisation of deformation and flow mechanics around porphyroblasts in a calcite marble ultramylonite by means of EBSD analysis. *Tectonophysics* 413, 185–200.
- Boese, C., Townend, J., Smith, E., Stern, T., 2012. Microseismicity and stress in the vicinity of the Alpine Fault, central Southern Alps, New Zealand. *J. Geophys. Res. Solid Earth* (1978–2012) 117 (B2).
- Brodie, K., Rutter, E., 2000. Deformation mechanisms and rheology: why marble is weaker than quartzite. *J. Geol. Soc.* 157, 1093–1096.
- Bunge, H.J., 1982. *Texture Analysis in Materials Science: Mathematical Methods*. Butterworths, London.
- Cande, S., Stock, J., 2004. Pacific–Antarctic–Australia motion and the formation of the Macquarie Plate. *Geophys. J. Int.* 157, 399–414.
- Cherniak, D., Watson, E., Wark, D., 2007. Ti diffusion in quartz. *Chem. Geol.* 236, 65–74.
- Dempsey, E.D., 2010. *The Kinematics, Rheology, Structure and Anisotropy of the Alpine Schist Derived Alpine Fault Zone Mylonites*, New Zealand (Ph.D. thesis). University of Liverpool.
- Eberhart-Phillips, D., 1995. Examination of seismicity in the central Alpine Fault region, South Island, New Zealand. *N. Z. J. Geol. Geophys.* 38, 571–578.
- Ellis, S., Stöckhert, B., 2004. Elevated stresses and creep rates beneath the brittle–ductile transition caused by seismic faulting in the upper crust. *J. Geophys. Res.* 109 (B05407).
- Ellis, S., Beavan, J., Eberhart-Phillips, D., Stöckhert, B., 2006. Simplified models of the Alpine Fault seismic cycle: stress transfer in the mid-crust. *Geophys. J. Int.* 166, 386–402.
- García Celma, A., 1982. Domainal and fabric heterogeneities in the Cap de Creus quartz mylonites. *J. Struct. Geol.* 4, 443–455.
- Ghent, E.D., Stout, M.Z., 1984. TiO_2 activity in metamorphosed pelitic and basic rocks: principles and applications to metamorphism in southeastern Canadian Cordillera. *Contrib. Mineral. Petrol.* 86, 248–255.
- Ghosh, S.K., 1975. Distortion of planar structures around rigid spherical bodies. *Tectonophysics* 28, 185–208.
- Gillam, B.G., Little, T.A., Smith, E., Toy, V.G., 2013. Extensional shear band development on the outer margin of the Alpine mylonite zone, Tatar Stream, Southern Alps, New Zealand. *J. Struct. Geol.* 54, 1–20.
- Gleason, G.C., Tullis, J., 1995. A flow law for dislocation creep of quartz aggregates determined with the molten salt cell. *Tectonophysics* 247, 1–23.
- Grapes, R.H., 1995. Uplift and exhumation of Alpine schist, Southern Alps, New Zealand: thermobarometric constraints. *N. Z. J. Geol. Geophys.* 38, 525–533.
- Griera, A., Llorens, M.G., Gomez-Rivas, E., Bons, P.D., Jessell, M.W., Evans, L.A., Lebensohn, R., 2013. Numerical modelling of porphyroblast and porphyroblast rotation in anisotropic rocks. *Tectonophysics* 587, 4–29.

- Grujic, D., Stipp, M., Wooden, J.L., 2011. Thermometry of quartz mylonites: importance of dynamic recrystallization on Ti-in-quartz reequilibration. *Geochem. Geophys. Geosyst.* 12 (6).
- Haertel, M., Herwegh, M., 2014. Microfabric memory of vein quartz for strain localization in detachment faults: a case study on the simplon fault zone. *J. Struct. Geol.* 68, 16–32.
- Haertel, M., Herwegh, M., Pettke, T., 2013. Titanium-in-quartz thermometry on synkinematic quartz veins in a retrograde crustal-scale normal fault zone. *Tectonophysics* 608, 468–481.
- Heilbronner, R., Tullis, J., 2006. Evolution of c axis pole figures and grain size during dynamic recrystallization: results from experimentally sheared quartzite. *J. Geophys. Res. Solid Earth* (1978–2012) 111 (B10).
- Hirth, G., Tullis, J., 1992. Dislocation creep regimes in quartz aggregates. *J. Struct. Geol.* 14, 145–159.
- Hirth, G., Teysier, C., Dunlap, J.W., 2001. An evaluation of quartzite flow laws based on comparisons between experimentally and naturally deformed rocks. *Int. J. Earth Sci.* 90, 77–87.
- Huang, R., Audétat, A., 2012. The titanium-in-quartz (TitaniQ) thermobarometer: a critical examination and re-calibration. *Geochim. Cosmochim. Acta* 84, 75–89.
- Humphreys, J., Bate, P., 2003. Gradient plasticity and deformation structures around inclusions. *Scr. Mater.* 48, 173–178.
- Jenkin, G., Craw, D., Fallick, A., 1994. Stable isotopic and fluid inclusion evidence for meteoric fluid penetration into an active mountain belt; Alpine Schist, New Zealand. *J. Metamorph. Geol.* 12, 429–444.
- Jochum, K.P., Nohl, U., Herwig, K., Lammel, E., Stoll, B., Hofmann, A.W., 2005. GeoREM: a new geochemical database for reference materials and isotopic standards. *Geostand. Geoanal. Res.* 29, 333–338.
- Kenkmann, T., Dresen, G., 1998. Stress gradients around porphyroclasts: palaeopiezometric estimates and numerical modelling. *J. Struct. Geol.* 20, 163–173.
- Kidder, S., Avouac, J.P., Chan, Y.C., 2012. Constraints from rocks in the Taiwan orogen on crustal stress levels and rheology. *J. Geophys. Res. Solid Earth* (1978–2012) 117 (B9).
- Kidder, S., Avouac, J.P., Chan, Y.C., 2013. Application of titanium-in-quartz thermometry to greenschist facies veins and recrystallized quartzites in the Hsüehshan range, Taiwan. *Solid Earth* 4, 1–21.
- Kidder, S., Toy, V., Prior, D.J., 2014. Transient stress magnitudes in the middle crust along the Alpine Fault. In: AGU Fall Meeting Abstracts.
- Kohlstedt, D., Evans, B., Mackwell, S., 1995. Strength of the lithosphere: constraints imposed by laboratory experiments. *J. Geophys. Res.* 100, 17–17.
- Koons, P., 1987. Some thermal and mechanical consequences of rapid uplift: an example from the Southern Alps, New Zealand. *Earth Planet. Sci. Lett.* 86, 307–319.
- Law, R.D., 2014. Deformation thermometry based on quartz <c> axis fabrics and recrystallization microstructures: a review. *J. Struct. Geol.* 66, 129–161.
- Law, R., Searle, M., Simpson, R., 2004. Strain, deformation temperatures and vorticity of flow at the top of the Greater Himalayan Slab, Everest Massif, Tibet. *J. Geol. Soc.* 161, 305–320.
- Law, R., Mainprice, D., Casey, M., Lloyd, G.E., Knipe, R., Cook, B., Thigpen, J., 2010. Moine Thrust Zone Mylonites at the Stack of Glencoul: 1—microstructures, Strain and Influence of Recrystallization on Quartz Crystal Fabric Development. In: Geological Society, London, Special Publications, vol. 335, pp. 543–577.
- Leitner, B., Eberhart-Phillips, D., Anderson, H., Nabelek, J., 2001. A focused look at the Alpine Fault, New Zealand: seismicity, focal mechanisms, and stress observations. *J. Geophys. Res.* 106, 2193–2220.
- Lister, G., Hobbs, B., 1980. The simulation of fabric development during plastic deformation and its application to quartzite: the influence of deformation history. *J. Struct. Geol.* 2, 355–370.
- Lister, G., Price, G., 1978. Fabric development in a quartz-feldspar mylonite. *Tectonophysics* 49, 37–78.
- Little, T., Holcombe, R., Ilg, B., 2002. Ductile fabrics in the zone of active oblique convergence near the Alpine Fault, New Zealand: identifying the neotectonic overprint. *J. Struct. Geol.* 24, 193–217.
- Liu, Z., Bird, P., 2002. Finite element modeling of neotectonics in New Zealand. *J. Geophys. Res. Solid Earth* (1978–2012) 107. ETG–1.
- Masuda, T., Ando, S., 1988. Viscous flow around a rigid spherical body: a hydrodynamical approach. *Tectonophysics* 148, 337–346.
- Menegon, L., Nasipuri, P., Stünitz, H., Behrens, H., Ravna, E., 2011. Dry and strong quartz during deformation of the lower crust in the presence of melt. *J. Geophys. Res. Solid Earth* (1978–2012) 116 (B10).
- Nachlas, W.O., Whitney, D.L., Teysier, C., Bagley, B., Mulch, A., 2014. Titanium concentration in quartz as a record of multiple deformation mechanisms in an extensional shear zone. *Geochem. Geophys. Geosyst.* 15, 1374–1397.
- Norris, R., Cooper, A., 2003. Very high strains recorded in mylonites along the Alpine Fault, New Zealand: Implications for the deep structure of plate boundary faults. *J. Struct. Geol.* 25, 2141–2157.
- Norris, R.J., Toy, V.G., 2014. Continental transforms: a view from the Alpine Fault. *J. Struct. Geol.* 64, 3–31.
- Passchier, C.W., Sokoutis, D., 1993. Experimental modelling of mantled porphyroclasts. *J. Struct. Geol.* 15, 895–909.
- Paterson, M., Luan, F., 1990. Quartzite Rheology Under Geological Conditions. In: Geological Society, London, Special Publications, vol. 54, pp. 299–307.
- Peterman, E.M., Grove, M., 2010. Growth conditions of symplectic muscovite + quartz: implications for quantifying retrograde metamorphism in exhumed magmatic arcs. *Geology* 38, 1071–1074.
- Price, G.P., 1978. Study of heterogeneous fabric and texture within a quartz-feldspar mylonite using the photometric method. *Geol. Soc. Am. Bull.* 89, 1359–1372.
- Prior, D.J., 1993. Sub-critical fracture and associated retrogression of garnet during mylonitic deformation. *Contrib. Mineral. Petrol.* 113, 545–556.
- Prior, D.J., Knipe, R.J., Handy, M.R., 1990. Estimates of the Rates of Microstructural Changes in Mylonites. In: Geological Society, London, Special Publications, vol. 54, pp. 309–319.
- Prior, D.J., Boyle, A.P., Brenker, F., Cheadle, M.C., Day, A., Lopez, G., Peruzzo, L., Potts, G.J., Reddy, S., Spiess, R., et al., 1999. The application of electron backscatter diffraction and orientation contrast imaging in the SEM to textural problems in rocks. *Am. Mineral.* 84, 1741–1759.
- Ramsay, J., 1980. Shear zone geometry: a review. *J. Struct. Geol.* 2, 83–99.
- Ranalli, G., 1984. Grain size distribution and flow stress in tectonites. *J. Struct. Geol.* 6, 443–447.
- Reed, J., 1964. Mylonites, cataclases, and associated rocks along the Alpine Fault, South Island, New Zealand. *N. Z. J. Geol. Geophys.* 7, 645–684.
- Samanta, S.K., Mandal, N., Chakraborty, C., 2002. Development of structures under the influence of heterogeneous flow field around rigid inclusions: insights from theoretical and numerical models. *Earth Sci. Rev.* 58, 85–119.
- Schmid, S., Casey, M., 1986. Complete fabric analysis of some commonly observed quartz c-axis patterns. *Geophys. Monogr. Ser.* 36, 263–286.
- Shigematsu, N., Prior, D., Wheeler, J., 2006. First combined electron backscatter diffraction and transmission electron microscopy study of grain boundary structure of deformed quartzite. *J. Microsc.* 224, 306–321.
- Sibson, R.H., 1974. Frictional constraints on thrust, wrench and normal faults. *Nature* 249, 542–545.
- Sibson, R., White, S., Atkinson, B., 1979. Fault rock distribution and structure within the Alpine Fault Zone: a preliminary account. *Orig. South. Alps* 18, 55–65.
- Sibson, R., White, S., Atkinson, B., 1981. Structure and Distribution of Fault Rocks in the Alpine Fault Zone, New Zealand. In: Geological Society, London, Special Publications, vol. 9, pp. 197–210.
- Sibson, R.H., Robert, F., Poulsen, K.H., 1988. High-angle reverse faults, fluid-pressure cycling and mesothermal gold-quartz deposits. *Geology* 16, 551–555.
- Skemer, P., Katayama, I., Jiang, Z., Karato, S.I., 2005. The misorientation index: development of a new method for calculating the strength of lattice-preferred orientation. *Tectonophysics* 411, 157–167.
- Spear, F.S., Ashley, K.T., Webb, L.E., Thomas, J.B., 2012. Ti diffusion in quartz inclusions: implications for metamorphic time scales. *Contrib. Mineral. Petrol.* 164, 977–986.
- Stern, T., Okaya, D., Kleffmann, S., Scherwath, M., Henrys, S., Davey, F., 2007. Geophysical Exploration and Dynamics of the Alpine Fault Zone. In: A Continental Plate Boundary: Tectonics at South Island, New Zealand, pp. 207–233.
- Stipp, M., Tullis, J., 2003. The recrystallized grain size piezometer for quartz. *Geophys. Res. Lett.* 30, 21.
- Stipp, M., Stuenkel, H., Heilbronner, R., Schmid, S.M., 2002. The eastern Tonale fault zone: a natural laboratory for crystal plastic deformation of quartz over a temperature range from 250 to 700 °C. *J. Struct. Geol.* 24, 1861–1884.
- Thomas, J.B., Watson, E.B., Spear, F.S., Shemella, P.T., Nayak, S.K., Lanzarotti, A., 2010. TitaniQ under pressure: the effect of pressure and temperature on the solubility of Ti in quartz. *Contrib. Mineral. Petrol.* 160, 743–759.
- Toy, V., Prior, D., Norris, R., 2008. Quartz fabrics in the Alpine Fault mylonites: influence of pre-existing preferred orientations on fabric development during progressive uplift. *J. Struct. Geol.* 30, 602–621.
- Toy, V., Craw, D., Cooper, A., Norris, R., 2010. Thermal regime in the central Alpine Fault Zone, New Zealand: constraints from microstructures, biotite chemistry and fluid inclusion data. *Tectonophysics* 485, 178–192.
- Toy, V.G., Prior, D.J., Norris, R.J., Cooper, A.F., Walrond, M., 2012. Relationships between kinematic indicators and strain during syn-deformational exhumation of an oblique slip, transpressive, plate boundary shear zone: the Alpine Fault, New Zealand. *Earth Planet. Sci. Lett.* 333, 282–292.
- Toy, V., Norris, R., Prior, D., Walrond, M., Cooper, A., 2013. How do lineations reflect the strain history of transpressive shear zones? the example of the active Alpine Fault Zone, New Zealand. *J. Struct. Geol.* 50, 187–198.
- Tullis, J., Yund, R.A., 1977. Experimental deformation of dry Westerly granite. *J. Geophys. Res.* 82, 5705–5718.
- Twiss, R.J., 1977. Theory and applicability of a recrystallized grain size paleopiezometer. *Pure Appl. Geophys.* 115, 227–244.
- Vry, J., Baker, J., Maas, R., Little, T., Grapes, R., Dixon, M., 2004. Zoned (Cretaceous and Cenozoic) garnet and the timing of high grade metamorphism, Southern Alps, New Zealand. *J. Metamorph. Geol.* 22, 137–157.
- Wark, D.A., Watson, E.B., 2006. TitaniQ: a titanium-in-quartz geothermometer. *Contrib. Mineral. Petrol.* 152, 743–754.
- White, S., 1977. Geological significance of recovery and recrystallization processes in quartz. *Tectonophysics* 39, 143–170.
- Woodcock, N., 1977. Specification of fabric shapes using an eigenvalue method. *Geol. Soc. Am. Bull.* 88, 1231–1236.